A scanning electron micrograph (SEM) of a micro-cantilever structure. The structure consists of a central rectangular frame with four cantilever arms extending outwards. The cantilevers are thin, rectangular beams. The central frame is more complex, with a central square opening. The entire structure is mounted on a substrate. The image shows the intricate details of the micro-fabrication process, including the sharp edges and the uniform thickness of the cantilevers.

Department of Precision and Microsystems Engineering

**Resonant modes of hollow micro-cantilevers for
characterization of liquids in picolitre volumes**

S.N.F. D Souza

Report no	2018.023
Coach	Dr. M.K. Ghatkesar
Professor	Prof. dr. U. Staufer
Specialisation	Micro and Nano Engineering
Type of report	Master thesis
Date	August 14, 2018

Resonant modes of hollow micro-cantilevers for characterization of liquids in picolitre volumes

by

S.N.F. D Souza

to obtain the degree of Master of Science
at the Delft University of Technology,
to be defended publicly on Tuesday August 28, 2018 at 09:00 AM.

Student number: 4616995
Project duration: September 14, 2017 – August 28, 2018
Thesis committee: Prof. dr. U. Staufer, Delft University of Technology
Dr. M. K. Ghatkesar, Delft University of Technology
Dr. F. Alijani, Delft University of Technology
Dr. P. Belardinelli, Delft University of Technology

An electronic version of this thesis is available at <http://repository.tudelft.nl/>.

Abstract

Micro and Nano-mechanical resonators are becoming increasingly ubiquitous in the areas of particle characterization and biological sensing. For biological sensing, however, the presence of a liquid environment is a pre-requisite. Hollow cantilevers, which allow fluids to be transported inside the resonator, often have high quality factors even when the channels are filled with fluids. This makes them attractive for both sensing mass and determining fluid properties in small volumes.

This work aims at determining the density of fluids in picoliter volumes with high resolution using hollow cantilevers. In order to achieve this, we obtain the resonance frequencies of the vibrating microstructure linked to three different modes: the first two flexural modes and the first torsional mode. The first torsional mode is unique to our device and is enabled by the specific geometry of the hollow cantilever.

Our approach involves filling the resonator channels with three different fluids in vacuum and monitoring the resonance frequencies and quality factors of the three modes. As the mode number increases, we observe that the shifts in resonance frequency and the quality factor for each liquid also increase. This implies that as we approach higher mode numbers there is an improvement in the sensitivity and resolution of the density measurement technique. The quality factors for the three fluids for a specific mode are not significantly different.

It is found that in order to achieve higher sensitivities and improved resolution in determining fluid properties, studying higher modes of hollow cantilevers in improved vacuum could indeed be an effective solution.

*S.N.F D Souza
Delft, August 2018*

Acknowledgements

The work presented in this thesis would not have been possible without the contribution of many others. I am indebted to all those with whom, I have had the pleasure to work, during the course of this year. This master thesis has been a wonderful learning experience for me.

Firstly, I would like to thank Farbod, Murali and Pierpaolo for introducing me to this project and their continuous support, knowledge and optimism. I would also like to thank Urs for his feedback at the pivotal moments in this project.

I would like to acknowledge Tomas and Mohammad for their input and suggestions. My sincere thanks also go to Harry, Patrick, Rob and Spiridon for their support in and around the lab.

Finally, to my parents, family and friends: for your constant encouragement and support, Thank You.

*S.N.F D Souza
Delft, August 2018*

Contents

List of Figures	ix
List of Tables	xi
1 Introduction	1
1.1 Suspended Microchannel Resonators	1
1.1.1 SMRs as biomechanical sensors	2
1.1.2 Working principle	3
1.2 Mass sensing with SMRs	4
1.3 Measuring fluid properties with SMRs	6
1.3.1 Measurement of pL fluid samples	6
1.3.2 Precision viscosity measurement with SMR	8
1.4 Quality factor	9
1.5 Summary	10
1.6 Research question	10
1.7 Measurement technique	10
1.8 Thesis outline	11
2 On the use of higher-modes of vibration for density measurements with fluid-filled hollow microresonators	13
3 Thermoelastic coupling effects on the natural frequencies	23
3.1 Mode shape imaging of hollow cantilevers	23
3.1.1 Mode shapes of hollow cantilevers in air	24
3.1.2 Mode shapes of hollow cantilevers in vacuum	24
3.2 Resonant frequency shift as a function of point location.	26
3.3 Measurement laser-induced frequency shift	29
4 Conclusion	33
5 Recommendations	35
A Setup fabrication	37
A.1 Vacuum compatible chamber.	37
A.2 Actuation	39
A.3 Height compensation	39
A.4 Conclusion	41
B Interface	43
B.1 Interfaces for two reservoir hollow cantilevers	43
B.2 Interfaces for new generation of two reservoir hollow cantilevers for dynamics experiments	44
B.3 Detailed views	45
B.3.1 Interfaces for two reservoir hollow cantilevers	45
B.3.2 Interfaces for new generation of two reservoir hollow cantilevers for dynamics experiments	45
C Additional Experimental data	47
C.1 Experiment 2	47
C.2 Experiment 3	49

D	Hollow cantilevers for dynamics experiments	51
D.1	No apertures at the tip of the cantilever	51
D.2	Wider cantilever legs	51
D.3	Reducing the number of bends of fluidic channels on the chips	52
D.4	Different lengths of cantilever.	52
E	Resonance frequency of hollow cantilevers with increasing laser power	55
F	Testing of AFM cantilevers in vacuum	57
G	Biomechanical sensors	61
	Bibliography	63

List of Figures

1.1	A typical Suspended Microchannel Resonator with the fluidic paths indicated in blue.	2
1.2	The limit of detection in moles (left axis) and grams per millilitre (right axis) versus the analysis time for the different types of biosensors.	2
1.3	Flow through mode with dilute solutions. The drop in resonance frequency when the particle is at the apex is evident.	3
1.4	(a) Optical microscope image of the chip with fluidic channels labelled (b) Packaging of the SMR labelled.	7
1.5	(a) Frequency vs density plots for the oil samples (b) Ratio of viscous damping of liquid to the damping of the empty cantilever versus the sample viscosity.	8
1.6	(a) Simultaneous change in frequency and amplitude when a fluid of lower viscosity and density replaces the existing fluid in the SMR (b) Plot of viscosity vs both Quality factor and Amplitude to compare the two methods.	8
1.7	Schematic of the basic components of a Laser Doppler Vibrometer.	11
3.1	Position of laser chosen for single point measurements.	23
3.2	First bending mode of the hollow cantilevers in air (134.5 kHz). The two images represent the two extremities of motion in this particular mode shape.	24
3.3	Second bending mode of the hollow cantilevers in air (828 kHz). The two images represent the two extremities of motion in this particular mode shape.	24
3.4	First torsional mode of the hollow cantilevers in air (916 kHz). The two images represent the two extremities of motion in this particular mode shape.	24
3.5	Mode shape linked to the peak in average spectrum of the hollow cantilevers in air (134.5 kHz). In the inset the mode shape associated with the first flexural resonant peak is shown.	25
3.6	Mode shape linked to the peak in average spectrum of the hollow cantilevers in air (828 kHz). In the inset the mode shape associated with the second flexural resonant peak is shown.	25
3.7	Mode shape linked to the peak in average spectrum of the hollow cantilevers in air (916 kHz). In the inset the mode shape associated with the first torsional resonant peak is shown.	25
3.8	Average spectrum zoomed in at Mode 1 in vacuum.	26
3.9	Average spectrum zoomed in at Mode 2 in vacuum.	26
3.10	Average spectrum zoomed in at Mode 3 in vacuum.	26
3.11	Frequency - Amplitude response of multiple points on one leg of the hollow cantilever at the first bending resonance frequency. Colour of the plots correspond to the colour of the dots on the hollow cantilever (inset).	27
3.12	Frequency - Amplitude response of multiple points on one leg of the hollow cantilever at the second bending resonance frequency. Colour of the plots correspond to the colour of the dots on the hollow cantilever (inset).	27
3.13	Frequency - Amplitude response of multiple points on one leg of the hollow cantilever at the first torsional resonance frequency. Colour of the plots correspond to the colour of the dots on the hollow cantilever (inset).	27
3.14	Experimental percentage relative frequency shift for mode 1, mode 2 and the torsional mode as we move away from the base of the cantilever (from left to right).	28
3.15	Temperature distribution with laser spot close to the tip of the leg.	30
3.16	Temperature distribution with laser spot close to the center.	30
3.17	Temperature distribution with laser spot about halfway between the center and the base.	30
3.18	Temperature distribution with laser spot close to the base.	30
3.19	Simulated vs experimental percentage relative frequency shift for mode 1, mode 2 and the torsional mode as we move away from the base of the cantilever (from left to right).	30
A.1	Isometric view of the basic components of the vacuum chamber.	37

A.2	Top view of the fluidic, electrical and vacuum attachments of the vacuum chamber.	38
A.3	Top and bottom view of the AFM cantilever holder. In the bottom view the blue squares denote magnetic connections and the red squares denote electrical connections.	39
A.4	(a)Flexible printed circuit to provide excitation to the holder (b) Marking of the pins to be connected for input voltage.	40
A.5	Three components used to simultaneously increase the height and house the FPC.	40
A.6	Final setup connected to all components.	41
A.7	(a) Connector compatible with vacuum tubing (b) Connector to block the hole in the chamber.	41
B.1	Interface for mounting and exchanging fluids with the chip.	43
B.2	Interface with chip mounted on the AFM holder.	44
B.3	Interface for mounting and exchanging fluids with the new chip.	44
B.4	Interface with new chip mounted on the AFM holder.	44
B.5	Orthographic views of the interfaces for hollow cantilevers.	45
B.6	Orthographic views of the interfaces for hollow cantilevers for dynamics experiments.	45
C.1	Resonance frequency shifts for the first bending mode in Experiment 2.	47
C.2	Resonance frequency shifts for the second bending mode in Experiment 2.	48
C.3	Resonance frequency shifts for the first torsional mode in Experiment 2.	48
C.4	Resonance frequency shifts for the first bending mode in Experiment 3.	49
C.5	Resonance frequency shifts for the second bending mode in Experiment 3.	49
C.6	Resonance frequency shifts for the first torsional mode in Experiment 3.	50
D.1	(a) Old cantilevers with aperture at tip marked by the red box (b) New cantilevers without aperture at tip. The tip region is marked by the red box. Both images taken at 20X magnification.	51
D.2	(a) Old cantilevers with laser positioned on one leg. Laser point is clearly as wide as the leg of the cantilever. (b) New cantilevers with laser positioned at tip. The laser is now smaller than the width of the leg. Both images taken at 20X magnification.	52
D.3	Old chip design for hollow cantilevers, the critical areas with respect to stress concentration are marked by the red boxes.	52
D.4	New chip design for hollow cantilevers, the new bends with large fillet radii are marked by the red boxes.	53
E.1	Shift in resonance frequency (measured) for the first bending mode plotted vs increasing laser power signal.	55
E.2	Shift in resonance frequency (measured) for the second bending mode plotted vs increasing laser power signal.	56
E.3	Shift in resonance frequency (measured) for the first torsional mode plotted vs increasing laser power signal.	56
E.1	Mode shape corresponding to Mode 1 in vacuum - AFM cantilever.	57
E.2	Average spectrum zoomed in at Mode 1 in vacuum - AFM cantilever.	57
E.3	Mode shape corresponding to Mode 2 in vacuum - AFM cantilever.	58
E.4	Average spectrum zoomed in at Mode 2 in vacuum - AFM cantilever.	58
E.5	Mode shape corresponding to Mode 3 in vacuum - AFM cantilever.	58
E.6	Average spectrum zoomed in at Mode 3 in vacuum - AFM cantilever.	58
E.7	Mode shape corresponding to Mode 4 in vacuum - AFM cantilever.	59
E.8	Average spectrum zoomed in at Mode 4 in vacuum - AFM cantilever.	59

List of Tables

1.1	Resonator and channel dimensions along with resonance frequencies.	4
1.2	Mass sensing achievements of SMRs to date.	5
1.3	Other related applications of SMRs.	6
A.1	List of parts of vacuum chamber.	37
A.2	List of added parts of vacuum chamber.	38
A.3	List of parts for height compensation.	40
C.1	Resonance frequency (f_{res}) and quality factors (QFs) for the first two bending and the first torsional mode for three experiments.	50
D.1	First four bending natural frequencies (f_1 , f_2 , f_3 and f_4) and the first torsional mode frequency (f_{tors}) for cantilevers with varying lengths simulated from COMSOL.	53
E.1	Resonant frequencies and quality factors of contact mode AFM cantilevers.	57

Introduction

Micro and Nano-mechanical resonators are becoming increasingly ubiquitous in the areas of biological sensing and the characterization of biological cells/molecules. These small scale resonators offer a label¹ free detection method while utilizing smaller sample volumes. Another advantage is that these detectors are also conveniently scalable (down-scalable in size and up-scalable in number) . All these factors greatly increase the throughput of sensing [2].

In the specific application of sensing mass, it is common to exploit the resonance frequency of the resonators. These characteristic frequencies are generally in the kHz [3, 4] - GHz [5] range. The detection sensitivity of the resonator, in the presence of an added mass, is directly proportional to the resonance frequency [6]. Since the presence of an added mass causes a shift in the resonance frequency, the high sensitivity required to sense a small specimen can only be achieved with high resonance frequencies. Also, the mass of the resonator and high quality factor are critical parameters for attaining higher sensitivities, and hence the most precise measurements to date have been achieved with the help of nano-mechanical resonators in vacuum [7]. These include the attainment of zeptogram resolution (10^{-21} g), in an ultra high vacuum apparatus with base pressure below 10^{-10} Torr [8] and the attainment of attogram resolution (10^{-18} g) in a vacuum chamber evacuated to a pressure of 3×10^{-6} Torr [9].

Micro/Nano resonators have been successfully used to measure the weight of single molecules [10], proteins [11] and nanoparticles [12]. The utility of these resonators is not limited to mass sensing, but they have also been employed to detect weak forces [13] and single molecule interactions [14]. In the grand scheme of things, nanomechanical resonators can serve as lab-on-a-chip biosensors enabling the early diagnostics of important diseases such as cancer [15].

1.1. Suspended Microchannel Resonators

Micro and Nano-mechanical resonators when operated in solutions suffer from a loss of Quality Factor (QF) and this directly translates to a degradation in frequency resolution. The drop in quality factor in a liquid environment is about two orders of magnitude when compared to a vacuum environment [17]. The sensing of biomolecules, in general involves fluid-structure interaction [18]. Additionally the presence of liquid environment is a requisite for bio-sensing applications. In order to make high resolution sensing possible in such situations, researchers (worth to mention Burg and Manalis [2]) suggested the creation of a channel for fluid flow in the cantilever, while ensuring that the cantilever itself is surrounded by air or vacuum. These cantilevers with fluid channels are referred to as Suspended Micro channel Resonators (SMRs) (a typical SMR can be seen in Figure 1.1). More commonly, in the absence of fluids, these resonators are simply called 'hollow cantilevers'. These dry resonators often have quality factors of upto 15000, and no decrease of quality factor is seen even with the addition of water in the channels [19]. The high resonance frequencies and high quality factors yield [20]:

¹A label is defined as any foreign molecule that is chemically or temporarily attached to the molecule of interest to detect molecular presence or activity, which can potentially alter its intrinsic properties [1].

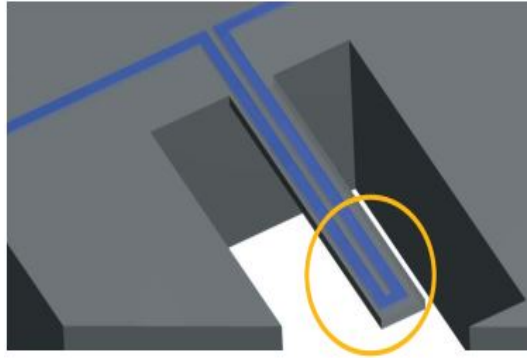


Figure 1.1: A typical Suspended Microchannel Resonator with the fluidic paths indicated in blue [16].

- high mass responsivity which is the frequency shift per added mass increment
- high frequency stability which is necessary to observe these mass induced frequency shifts.

1.1.1. SMRs as biomechanical sensors

In general, bio-mechanical sensors can be classified as:

- Surface stress mechanical biosensors, which measure the quasistatic deflection of the cantilever, caused by the surface binding of biomolecules with functional groups on the surface of the cantilever.
- Dynamic mode mechanical biosensors in which the devices are excited at their resonance frequencies. The shift in resonance frequency in the presence of a biomolecule is measured [21]. SMRs fall into this category.

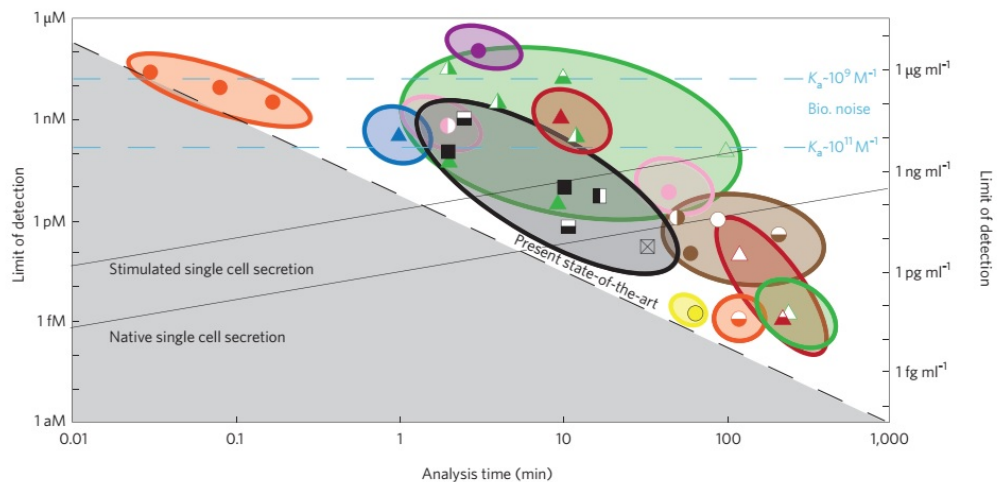
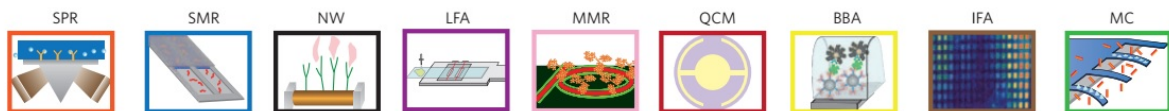


Figure 1.2: The limit of detection in moles (left axis) and grams per millilitre (right axis) versus the analysis time for the different types of biosensors shown in the legend at the top of the figure [21]. Note : Both scales in the figure are logarithmic. In the figure, the abbreviations can be expanded as : SPR-Surface Plasmon Resonance, SMR-Suspended Microchannel Resonators, NW-Nanowires, LFA-Lateral Flow Assay, MMR-Microring Resonator, QCM-Quartz Crystal Monitor, BBA BioBarcode Amplification Assay, IFA - Immunofluorescent Assay and MC- Microcantilevers (See Appendix G).

An ideal biosensor, would offer both lower limits of detection in terms of concentration and shorter detection times (preferably less than one minute) simultaneously. In a graph with increasing detection times on the

x-axis and increasing limits of detection on the y-axis, one would expect the most desirable sensors to occupy the bottom left area. Figure 1.2 plots the above mentioned parameters on the x- and y- axis. From the plot, we can clearly see why SMRs are preferred for quick and easy detection. The analysis time is close to the desired value of a few minutes (~ 1 min) and they offer considerably good levels of detection (~ 300 pM).

1.1.2. Working principle

If particles suspended in a solution are allowed to continuously flow through the resonator, as each particle flows through, it induces a frequency shift which is dependent on the mass of the particle and its position in the SMR [19]. For dilute solutions, the peaks in a frequency vs time plot are well separated, and the height of each of these peaks (frequency shift) is directly proportional to the mass of the particle flowing through. The exact mass excess of the particle in the resonator can be quantified by the frequency shift induced when the particle is at the apex (See Figure 1.3). This measurement mode is known as the flow through mode/ flow through detection mode.

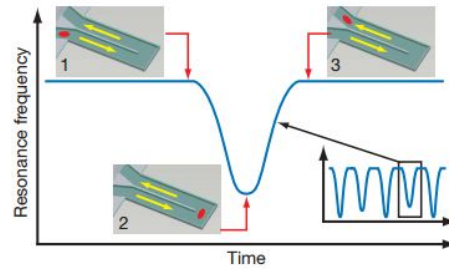


Figure 1.3: Flow through mode with dilute solutions. The drop in resonance frequency when the particle is at the apex is evident [19].

The other measurement method is affinity based capture, which generally is more practical for the smallest targets, as the device needs to be less sensitive and time averaging enables more precise detection [20]. In this method, the inner channel walls are functionalized. When the solution containing the biomolecules (to be detected) flows through the channels of the resonator, the biomolecules bind at the available sites. The presence of these biomolecules at the binding sites increases the effective mass of the resonator thereby inducing a frequency shift, which can be measured over time.

The relation linking changes in mass to the subsequent new frequency in the flow through method is given by Equation 1.1 [19]:

$$f_{new} = \frac{1}{2\pi} \sqrt{\frac{k}{m^* + \alpha \Delta m}} \quad (1.1)$$

where k is the spring constant of the SMR, m^* is the effective mass, α is a constant which depends on the geometrical localization of the added mass Δm . In the special case of the particle in transit being positioned at the apex, α assumes the value 1.

Suspended microchannel devices actually sense changes in relative density, that is, of the relative increase in mass over that of the fluid displaced by an analyte, which is essentially the mass difference [20].

In principle, SMRs can provide high sensitivities for mass detection, and the argument motivating the use of SMRs in mass sensing applications for early detection is valid. However in practical implementations, SMRs have constraints on the maximum volume of fluid that can flow through a narrow channel at tolerable operating pressures. An additional issue is the relatively small amount of time the particle lies within the cantilever channel [20].

In theory, for flow through detection, the requisite fractional shift in frequency to achieve a detectable mass shift can be given by [22, 23]:

$$\frac{\partial f}{f} = \frac{1}{2Q[SMR]} = -\frac{\partial m_{min}}{2M_{eff}} \quad (1.2)$$

where f is the resonance frequency of the SMR, Q is the quality factor, M_{eff} is the effective mass of the device including the fluidic mass loading and m_{min} is the mass difference (described in the previous section). This frequency shift is highly dependent on the particle position along the channel length, with the highest sensitivities obtained at the tip of the cantilever [19]. This relationship clearly shows that at higher frequencies of the resonators even smaller masses can be detected.

1.2. Mass sensing with SMRs

Table 1.2 summarizes the existing work involving suspended microchannel resonators, the type of particles used, and the mass detected. The resonator and channel dimensions along with the resonance frequencies (if reported) of the SMRs can be seen in Table 1.1. In a separate experiment (Table 1.3) the SMRs have also been employed to determine the average diameter. Generally, gold nanoparticles and polystyrene beads are used for calibration. More recently, SMR arrays with delay channels have been used for high throughput measurements of single cell growth rate [24]. The discussions here, are however, limited to standalone SMR devices.

Table 1.1: Resonator and channel dimensions along with resonance frequencies.

Application	Resonator dimensions	Channel dimensions	Resonance frequencies
Gold nanoparticles, Polystyrene microspheres, E.coli and B.subtilis [19]	200 μm (length) \times 33 μm (width) \times 7 μm (height)	3 μm (height) \times 8 μm (width)	220.5 kHz with air in channels and 209.6 kHz with water in channels
Avidin [2]	300 μm length	Wall thickness - 800 nm	42.7 kHz with air in channels, 40.1 kHz with 2-Propanol in channels and 39.6 kHz with water in channels
Gold nanoparticles [7]	50 μm (length) \times 10 μm (width) \times 1.3 μm (height)	2 μm wide and 700 nm high. Total length of buried nanochannel = 375 μm	Theoretical resonance frequency - 784 kHz Measured resonance frequency - 665 kHz
Gold nanoparticles, Polystyrene beads, Exosomes, DNA origami and gold nanoparticles assembly [12]	50 μm (length) \times 10 μm (width) \times 1 μm (height)	400 nm high and 2 μm wide	Theoretical resonance frequency - 589 kHz
	37.5 μm (length) \times 7.5 μm (width) \times 1 μm (height)	400 nm high and 1 μm wide	Theoretical resonance frequency - 1.03 MHz
	27 μm (length) \times 7.5 μm (width) \times 1 μm (height)	400 nm high and 1 μm wide	Theoretical resonance frequency - 1.99 MHz
	22.5 μm (length) \times 7.5 μm (width) \times 1 μm (height)	400 nm high and 1 μm wide	Theoretical resonance frequency - 2.87 MHz

Table 1.2: Mass sensing achievements of SMRs to date.

Application	Frequency shift known/detected	Mass known/detected	Size	Miscellaneous information
Gold nano-particles [19]	36 mHz	10 fg	100 ± 8 nm	Calibration for later biological detection. Flow through detection.
Polystyrene micro spheres [19]	310 mHz	90.1 fg	1.51 ± 0.01 μ m	Calibration for later biological detection. Flow through detection.
E. coli bacteria [19]	≈ 400 mHz	110 ± 30 fg	0.8×2 μ m Rod	Low flow rate of 10–100 pl/s that is required for femtogram resolution limits throughput to 1–10 particles per second. Flow through detection.
B. subtilis bacteria [19]	≈ 500 mHz	150 ± 40 fg	1×2.5 μ m Rod	Low flow rate of 10–100 pl/s that is required for femtogram resolution limits throughput to 1–10 particles per second. Flow through detection.
Avidin [2]	Not reported	1.4×10^{-17} g/ μ m ²	Not reported	Used for biomolecular detection. Affinity based capture. Frequency shift of 1-3 kHz with different fluids in SMR.
Gold nano-particles [7]	≈ 1.2 Hz	Buoyant mass ≈ 1.2 fg	50 nm	100 ms transit time through the channel at 10 kPa pressure difference. Inertial trapping of particles to employ averaging techniques.
Gold nano-particles [7]	≈ 0.1 Hz	Buoyant mass ≈ 77 ag in water	20 nm	Data from five consecutive trapping exercises.
Polystyrene particles [25]	≈ 0.62 Hz - 0.66 Hz	Buoyant mass ≈ 165 fg - 177 fg	1.9 μ m	32000 consecutive measurements over 20 hours.
Bare particles Polystyrene [26]	Not reported	Buoyant mass $\approx 33.30 \pm 0.07$ fg	1000 nm	Measurement time of 10 minutes allows 2000 particles to be measured.
Protein coated particles (Polystyrene) [26]	Not reported	Buoyant mass $\approx 34.50 \pm 0.25$ fg	1000 nm	Measurement time of 10 minutes allows 2000 particles to be measured.

Table 1.3: Other related applications of SMRs.

Application	Experimentally predicted values (diameters/ concentration/ buoyant mass).	Actual values (diameters/ concentration/ buoyant mass).	Miscellaneous information
Gold nanoparticles [12]	9.9 nm 14.4 nm 19.7 nm	9.9 nm 14.3 nm 20.4 nm	Calibration for later detection. 97 minute experiment to measure roughly 29000 particles.
Polystyrene beads [12]	150 nm 200 nm 220 nm	149.8 nm 14.3 nm 20.4 nm	Calibration for later detection. 30 minute experiment to measure roughly 12500 particles. Average transit time per particle is about 30 ms.
Exosomes [12]	10^9 particles/mL 10^{10} particles/mL 10^{11} particles/mL 44.6 nm(type-1) 44.1 nm(type-2)	10^9 particles/mL 0.9×10^{10} particles/mL 0.4×10^{10} particles/mL ≈ 46.6 nm(type-1) ≈ 45.0 nm(type-2)	Probability of detection is 1 for exosomes with a buoyant mass greater than 10 ag.
DNA origami and gold nanoparticles assembly [12]	30 ag	Not reported	Flow rate of approximately 3 nL/hr.

1.3. Measuring fluid properties with SMRs

As is evident from the previous section, the development of SMRs has made it possible to measure masses at attogram/femtogram resolution in fluid environment. And it is in such applications that their ultimate utility is to be found. But the fact that these devices exhibit no appreciable loss of quality factor even after the channels are filled, makes SMRs extremely suited for measuring fluid properties, namely density (which can be directly linked to the resonance frequency) and viscosity (which can be linked to the quality factor or amplitude). In the following sub-sections such applications are discussed briefly.

1.3.1. Measurement of pL fluid samples

The SMR is able to measure density of individual fluids effectively, however there are variety of errors and deviations involved when different SMRs have to be used while measuring multiple fluids. For example each device has slightly varying resonance frequencies or quality factors. Transparent channels in the SMR provide two distinct advantages. Visual inspection is possible for the presence of air bubbles, blocked channels and remains of previous samples in the channel. Secondly, it provides a cost effective alternative wherein the SMRs can be used for multiple measurements with different fluids [27].

Device design

The cantilever resonator is 20 μm wide and 200 μm long. The transparent fluidic channels are 4 μm by 3 μm , which is similar to the channel dimensions (3.7 μm by 2.2 μm) we propose to use. The channels that deliver and rinse the fluid out of the SMR, are named as SDC- sample delivery channels (See Figure 1.4 (a)). Each SDC is 150 μm wide and approximately 2300 μm long. The SDC is connected to macro sized fluid tubings through the back side of the chip. The packaging around the device mainly consisted of an aluminium lid at the top of the chamber and a window for optical readout. At the bottom a polyetheretherketone (PEEK) fixture housed the piezo-actuator, microfluidic connections and a temperature sensor. The vacuum chamber kept the pressure at approximately 10^{-5} mbar (See Figure 1.4 (b)) [27]. We expect to work at much higher pressures (roughly 1 mbar). As a direct consequence we expect our quality factor to be significantly lower.

⁰1 fg = 10^{-15} g

⁰1 ag = 10^{-18} g

⁰Buoyant mass = Volume of the particle times difference in densities of particle and fluid [25]

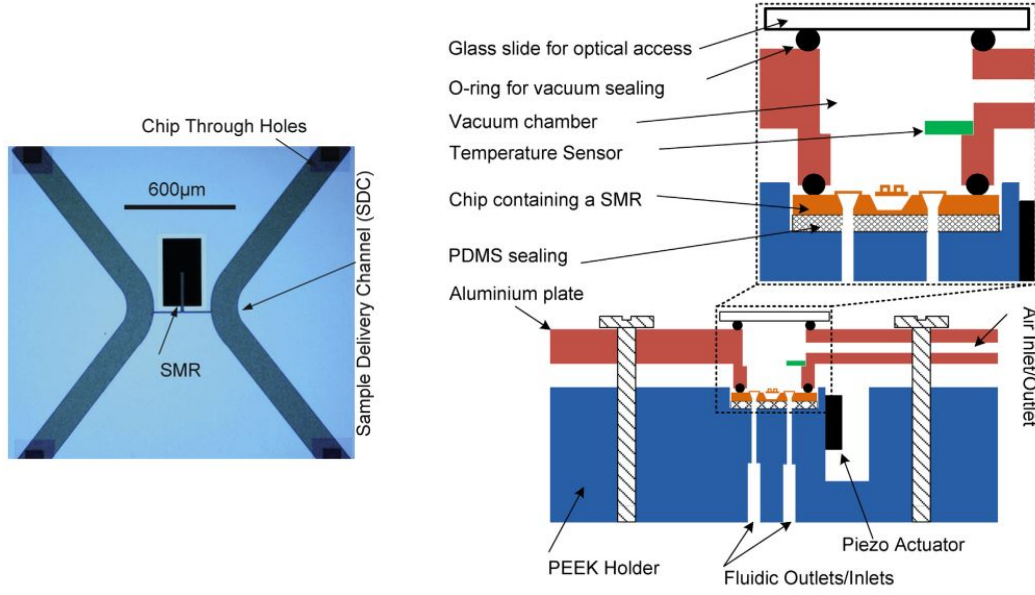


Figure 1.4: (a) Optical microscope image of the chip with fluidic channels labelled (b) Packaging of the SMR labelled [27].

Theoretical model to determine viscosity

The fluid inside the SMR can be assumed to be homogeneously loading the cantilever beam. For low damping, the measured resonance frequency (ω_r) can be assumed to be equal to the undamped eigen frequency (ω_o) and

$$\omega_o = \omega_r = \sqrt{\frac{k}{m}} = \sqrt{\frac{k}{m_c + m_f}} = \sqrt{\frac{k}{V_c \rho_c + V_f \rho_f}} \quad (1.3)$$

where k is the spring constant, m is the mass, m_c is the mass of the cantilever and m_f is the mass of the fluidic loading. V and ρ are the associated volumes and mass densities.

Under the assumption that the fluid does not change the stiffness of the cantilever, Equation 1.3 can be rewritten as [27]:

$$\omega_r = \frac{A}{\sqrt{B + \rho_f}} \quad (1.4)$$

where A , B are constants that can be determined from the resonance frequency measurements of two different fluids with known standard mass densities.

And the density of the fluid to be determined (ρ_f) is given by:

$$\rho_f = \left(\frac{A}{\omega_r}\right)^2 - B \quad (1.5)$$

Also it is possible to relate the viscous damping coefficient of the fluid to the viscous damping coefficient of the empty cantilever, this ratio is given by C_f/C_c .

Finally the damping of the fluid to be determined is given by [27]:

$$\frac{C_f}{C_c} = \frac{\omega_{r,air} Q_{air}}{\omega_f Q_f} - 1 \quad (1.6)$$

where C_f is the damping of the fluid, C_c is the damping of the cantilever and Q is the quality factor in the respective media.

Measurements

The resonator was driven by a piezo actuator in the linear regime. The resonance frequency was measured with a laser Doppler vibrometer with twenty times averaging. The resonance frequency and quality factor were then extracted from the resonance peak. Calibration was done by measuring the cantilevers with two fluids with well established densities, air and water. The SMR has a sensitivity of 16 Hz/kg/m^3 .

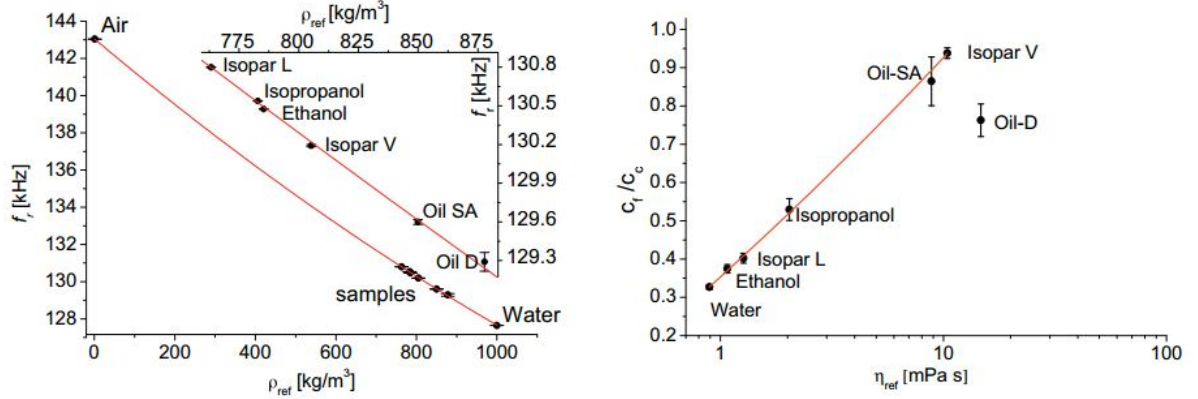


Figure 1.5: (a) Frequency vs density plots for the oil samples (b) Ratio of viscous damping of liquid to empty microchannel versus the sample viscosity [27].

The four oil samples were loaded into the SMR one after another. Rinsing the channels with toluene and flushing with acetone before changing the fluids, helped clean the channels before subsequent measurements. Before starting a measurement each sample was kept in the channel for four minutes until flow and thermal stability is achieved. The viscosity of the solutions were simultaneously measured with an accuracy of 0.025 mPa s (by measuring the quality factor in the presence of fluids). Results obtained from these curves matched well with data achieved from commercial density and viscosity meters [27].

1.3.2. Precision viscosity measurement with SMR

For precision viscosity measurements two methods are introduced [28]:

- Quality factor based (ΔQ in Figure 1.6)
- Amplitude based (ΔA in Figure 1.6)

It has already been established in the work of Sader et al [29], that the relationship between quality factor and viscosity is non monotonic. Hence, the authors choose to characterize a narrow range of viscosities (1-10 mPa s).

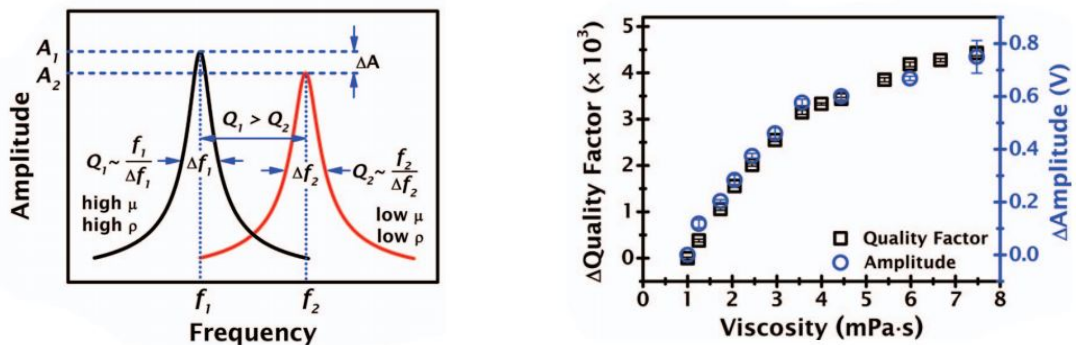


Figure 1.6: (a) Simultaneous change in frequency and amplitude when a fluid of lower viscosity and density replaces the existing fluid in the SMR (b) Plot of viscosity vs both Quality factor and Amplitude to compare the two methods [28].

Two main observations can be made from Figure 1.6:

- The quality factor increases by about 4000 for a 7 mPas increase in viscosity.
- The quality factor increases more rapidly for a unit change in viscosity of the liquid at lower viscosities when compared to slightly higher viscosities.

The increase in quality factor when filled with fluids of higher viscosity is contradictory to what is observed in the case of micro cantilevers surrounded by fluid [30]. Manalis et al argue that when the devices are empty (filled with air) the dissipation is dominated by the energy loss of the solid resonator. This determines the quality factor. However, when filled with liquid, shear induced damping lowers the quality factor while the added mass due to the fluid increases the energy storing capacity of the beam. These phenomenon act simultaneously to result in no change or an increase in quality factor when the resonator is filled with fluid [7].

The quality factor can be calculated as the ratio of the resonance frequency to the difference between frequencies at the half power point. So, the resonance frequency itself should affect the quality factor of the SMR when a new fluid enters the SMR. It has been established experimentally that the resonance frequency is inversely proportional to the density of fluid in the channel [7]. Hence, if the effect of resonance frequency is minimal, the effect of density can be considered minimal too. To test this theory, two fluids with similar viscosities but different densities are chosen. The quality factors when these two fluids are passed through the SMR at varying temperatures, are similar. This means in the small tested range, the viscosity can be linked to the quality factor without accounting for corrections owing to the density [7].

1.4. Quality factor

In the two techniques used to determine viscosity and the methods used to sense mass using these devices, the quality factor of the resonator is central to the discussion. The quality factor indicates the sharpness of peak at resonance. The Lorentzian function can be used to approximate the frequency amplitude response in the case of slightly damped systems. The determination of amplitude of the peak is not always straightforward to determine. Another way is to measure the slope of the phase-frequency response. If we use the phase to determine the quality factor, the quality factor (Q) can be given by the following equation [31]:

$$Q \approx \frac{\Omega}{2} \left(\frac{\partial \phi}{\partial \omega} \Big|_{\omega=\Omega} \right) \quad (1.7)$$

where ϕ represents the phase, ω the frequency and Ω the resonance frequency.

In general the total quality factor is linked to the quality factors arising from various different dissipation mechanisms. The total quality factor is hence:

$$\frac{1}{Q} = \frac{1}{Q_{medium}} + \frac{1}{Q_{clamping}} + \frac{1}{Q_{intrinsic}} + \frac{1}{Q_{other}} \quad (1.8)$$

where,

- Q_{medium} reflects all the losses that occur when a fluidic medium interacts with the mechanical device.
- $Q_{clamping}$ reflects all the energy lost from the device at the clamping sites.
- $Q_{intrinsic}$ reflects all dissipation mechanisms in the bulk of the resonator, on the surface of the resonator and within the resonator itself.
- Q_{other} is representative of all loss mechanisms not covered in the first three [31].

In the work involving quality factors of SMRs which use the theoretical model defined in [32], the quality factor is assumed to be only dependent on Q_{int} and Q_{fluid} . Here, Q_{int} also includes the previously mentioned

⁰ $Q_{intrinsic}^{air}$ refers to the intrinsic quality factor when air is present in the channels. Q_{fluid}^{water} refers to the quality factor due to the fluid when water is present in the channels.

$Q_{clamping}$ and Q_{other} . And Q_{fluid} is the quality factor due to fluid presence in the channels. This implies the total quality factor equation reduces to:

$$\frac{1}{Q} = \frac{1}{Q_{int}} + \frac{1}{Q_{fluid}} \quad (1.9)$$

The intrinsic quality factor (Q_{int}) is assumed to be frequency independent and hence when the channels are filled with water, it merely scales as a function of the mass added and Q_{int}^{water} is much greater than Q_{int}^{air} . However Q_{fluid}^{air} is very large compared to Q_{int}^{air} . And hence for the case of a channel with only air, the resulting quality factor is mainly determined by Q_{int}^{air} . For the case of water, both Q_{fluid}^{water} and Q_{int}^{water} have comparable magnitudes and hence the effective quality factor is lower than Q_{int}^{water} [32].

1.5. Summary

The miniaturization of fluidic channels of the suspended resonators from the micro-scale to nano-scale helped push the barriers of mass sensing with these resonators. The latest generation of SNRs are capable of attogram sensing. This was brought about by the advancements in fabrication technology and improved packaging techniques which helped decrease the mass of the resonators and achieve high vacuum levels respectively.² As the devices become smaller, the detection and frequency tracking schemes to track the shifts in frequencies associated with smaller masses become more complex too. The limits of detection at this point are not only influenced by the device performance but by the performance of the read out circuitry. In an attempt to achieve optimum frequency stability the cantilevers are being excited at higher amplitudes. This higher excitation was made possible by switching to piezoceramic based actuation. Alternate detection schemes based on piezoresistive sensing can offer some reduction in the complexity associated with optical elements. In the meanwhile, both the understanding and theoretical models of the underlying physics are also improving. Improvements on all these fronts can ultimately help SMRs/SNRs compete with conventional techniques as they can massively reduce processing times for sample studies.

1.6. Research question

It is now evident that the behaviour of devices with embedded fluidic channels in them, depends on a variety of factors including channel height and width, the ratio of the channel dimensions with respect to the cantilever dimensions and how accurately the channel can be positioned in the cantilever during fabrication. It is therefore essential to characterize these empty devices first and to then observe the effect of filling fluids in the channels on various modes of these hollow cantilevers. Finally, the research question can be formulated as:

'What is the smallest density change that can be experimentally determined using hollow cantilevers fabricated at TU-Delft?'

Since, the focus of this project extends beyond the fundamental mode of hollow cantilevers, the aim is to also be able to answer the question:

'What is the improvement in resolution and sensitivity (if any) when higher modes are used for the determination of density?'

1.7. Measurement technique

The actuation and detection of the amplitude of the deflection of the hollow cantilever can be done in multiple ways. The actuation can be done by either electrostatic or piezoelectric means. Further details about the actuation can be found in Appendix A. In this section we briefly describe the detection method.

In order to measure the deflection of the hollow cantilever, we use an optical detection method implemented on a Polytec Laser Doppler Vibrometer (LDV). The output beam of a 633 nm He-Ne laser is split into two

² It is necessary to keep in mind that some applications, such as that of studying the growth of mammalian cells, demand larger channel dimensions [29]. This means that channel dimensions are to be decided based on the possible application.

beams: the reference and the test beam. The test beam is then reflected back from the device under test and directed by a beam splitter to finally merge with the reference beam (and towards the detector). For every displacement equal to half the laser wavelength, one complete dark/light circle is observed. The Bragg cell typically modulates the light frequency by a set amount so that the direction of movement of the device can also be detected.

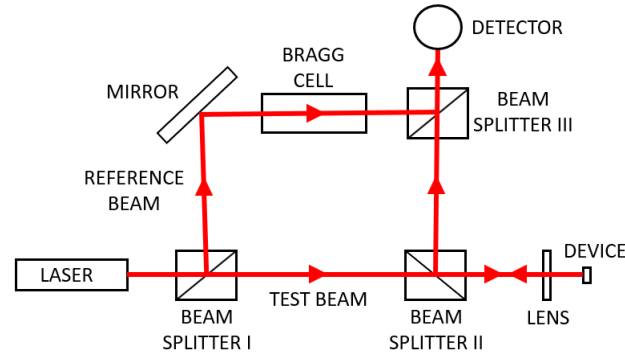


Figure 1.7: Schematic of the basic components of a Laser Doppler Vibrometer.

1.8. Thesis outline

Following the introductory chapter, which elaborates on the motivation behind this project and the current state of the art in the field of SMRs, the main contents are presented in paper format in Chapter 2. In Chapter 3, the effects induced by the measurement laser on the hollow cantilever are discussed. The chapter titled 'Conclusions' finally summarizes the findings of this project. Chapter 5 covers some recommendations on various aspects of the project. For completeness and further reference, a discussion on the setup and its fabrication can be found in Appendix A, the interfacing of the cantilevers with the macro world in Appendix B, some important experimental data (additional) can be found in Appendix C and details of the new generation of hollow cantilevers in Appendix D. In Appendix E, F and G the effect of laser power on the frequency measurement, experiments linked to mode shape imaging of atomic force microscope cantilevers and some other biomechanical sensors are respectively briefly discussed.

2

Paper

On the use of higher-modes of vibration for density measurements with fluid-filled hollow microresonators

S.N.F. D Souza¹, P. Belardinelli¹, E. Verlinden¹, J. Wei², U. Staufer¹, F. Alijani¹ and M.K. Ghatkesar¹

¹Department of Precision and Microsystems Engineering, TU Delft, Netherlands

²Department of Microelectronics, TU Delft, Netherlands

August 14, 2018

Hollow cantilevers with high quality factors facilitate sensing in liquid environments. To detect small density changes accurately it is important to improve the sensitivity and resolution of density measurements. We present a method to achieve this by exploiting higher modes of vibration of hollow cantilevers. Our work aims at studying the behavior and sensing characteristics of the hollow cantilever vibrating in three different modes: the first two bending modes and the first torsional mode. The latter is enabled by the unique geometry of the proposed device. The experiments are performed with three liquids with different densities. The measurements with the torsional mode highlight an improvement of about six times in the sensitivity and about fifteen times in the resolution of density estimation when compared to the fundamental mode of the cantilever. In conclusion, this method of studying higher modes of hollow cantilevers could be an effective solution to detect small density changes even in high vacuum.

1 Introduction

The ability to measure density accurately is crucial in a variety of industries. Density measurements are

ubiquitous in the biomedical [1], chemical [2] and petroleum [3] industries. Most of these applications still rely on conventional density detecting principles and instrumentation which make use of large volumes of fluids. Thus, this represents a severe limitation in situations wherein large amounts of fluid are either too expensive or difficult to obtain. This problem can be circumvented by the use of microcantilevers, which use appreciably smaller fluid volumes [4], [5].

Microcantilevers are typically excited at their resonance frequency, and when surrounded by a fluid, the shift in the resonance frequency of the cantilever can be exploited for sensing applications [7]. A major drawback of operating in solution is the presence of high damping or in other words the conspicuous loss of Quality Factor (QF) which corresponds to a degradation in frequency resolution. As a matter of fact, the drop in QF in a liquid environment is about two orders of magnitude when compared to operation in vacuum [8].

In order to make high resolution sensing possible in such situations, Burg and Manalis [9] suggested the creation of a channel for fluid flow inside the cantilever, while ensuring that the cantilever itself is surrounded by air or vacuum. More commonly, in the absence of fluids, these resonators are simply called 'hollow cantilevers'. These dry resonators often have QFs of upto

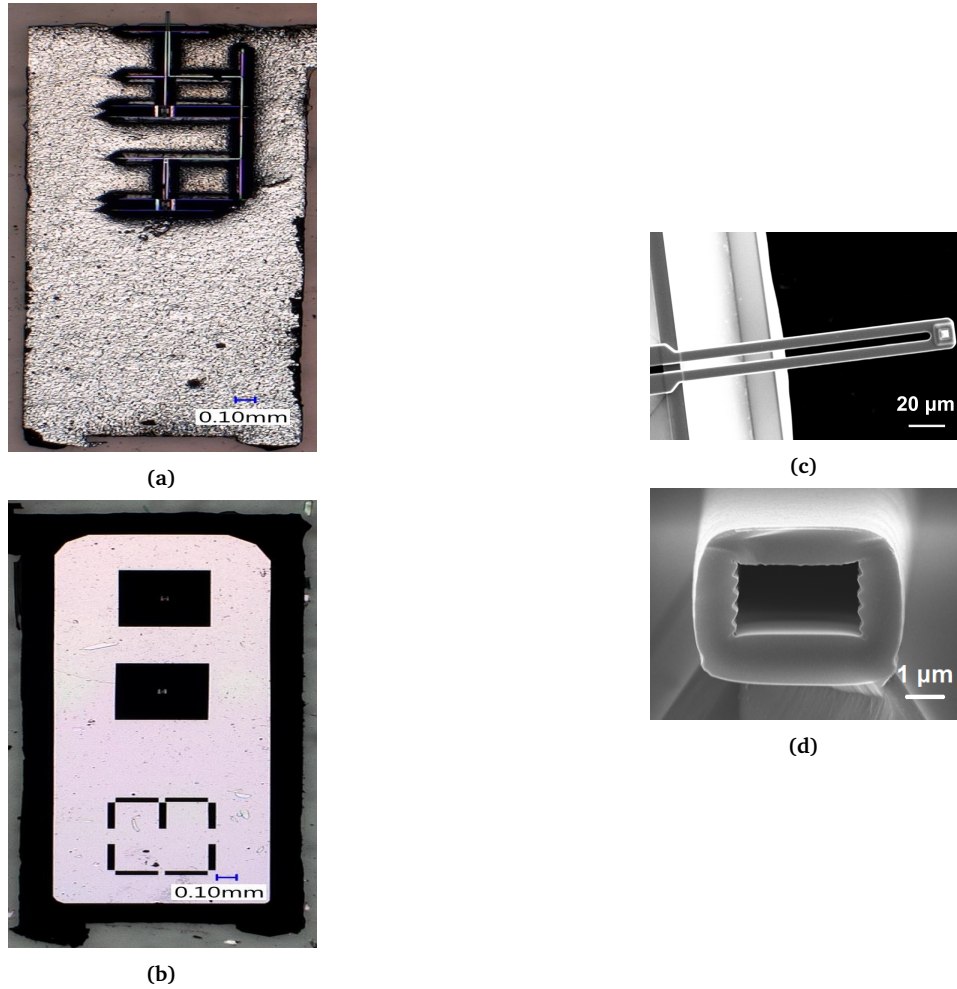


Figure 1: (a) Optical micrograph of the chip with the hollow cantilever at the top; (b) optical micrograph of the back side of chip with the two reservoirs; (c) scanning electron micrograph of the hollow cantilever; (d) cross section of the $\sim 3.7\mu\text{m} \times 2.2\mu\text{m}$ fluidic channel embedded in the cantilever [6].

15000 (in vacuum), and no significant change in QF is seen in the fundamental resonance curve even with the addition of water in the channels [10]. There are various instances of density measurements using these novel devices. Density measurements have been conducted to characterize sticky and viscous oil samples [2] or to study the performance of the device before sensing mass [9], [11]. In these applications, two attributes of these devices are important: frequency stability and high sensitivity [12]. Frequency stability implies that the deviations from the resonance frequency must be as low as possible. This helps in detecting the small frequency shifts due to the changes in density. Higher sensitivities mean that the shift in resonance frequency per unit increase in density is also relatively higher. To be able to sense the smallest changes in density (due to the presence of nano particles or biological media) accurately, it is important to improve on both these aspects.

In this work we aim to do that by analyzing the first two bending modes and a torsional mode of vibration of the hollow cantilever in the presence of fluid. We

show that these higher modes of vibration improve the performance of the device and achieve higher density sensitivity and better resolution.

2 Device Details

Table 1: Device dimensions

Parameter	Value(in μm)
Cantilever length	155
Cantilever width	16
Cantilever height	4.9
Cantilever Leg width	5
Gap between the two legs	6
Fluidic channel height	2.2
Fluidic channel width	3.7
Chip length	3030
Chip width	1100
Chip height	250

The device used in this work is a hollow cantilever made of silicon dioxide (Figure 1a) [13]. The cantilever is connected to two reservoirs on the chip. Figure 1b shows the two reservoirs on the back side of the chip. The resonator presents a particular geometry in which the inlet and outlet legs are separated and free to oscillate in counterphase (Figure 1c). Figure 1d shows the fluidic channel embedded in the cantilever that allows the fluid to flow. The dimensions of the hollow cantilever and the chip can be found in Table 1.

2.1 Fluid Interface

A continuous flow in the hollow cantilever is maintained by supplying an on-chip etched reservoir ($450\mu\text{m} \times 450\mu\text{m}$) with the desired fluid. Another on-chip reservoir continuously collects the fluid that has passed through the hollow cantilever. These on-chip reservoirs were able to continuously exchange fluids with the macro world through a 3-D printed interface. The interfaces were made on a $25\mu\text{m}$ resolution printer (Envisiontec Micro Plus Hires) using acrylic resins. The reservoirs of the chip were precisely aligned with the reservoirs on the interface before the chip and interface were glued together. Figure 2 shows a schematic of the chip aligned with the interface. The fluidic samples were provided to the printed interface by Tygon tubing (inner diameter: 0.25 mm) and general purpose dispense tips (outer diameter : 0.24 mm).

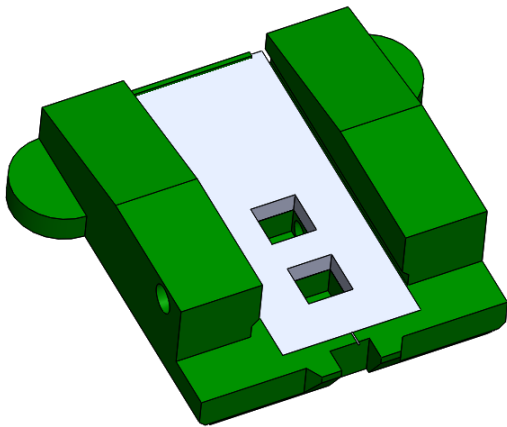


Figure 2: Chip (in white) placement on the interface (in green). The reservoirs on the chip have been cut through the whole section intentionally to show alignment with the reservoirs on the interface. In reality the top part of the chip is as in Figure 1a.

3 Modal analysis/ vibration testing

3.1 Setup

Since detection in hollow cantilevers is based on frequency monitoring, higher Q-factors can improve the

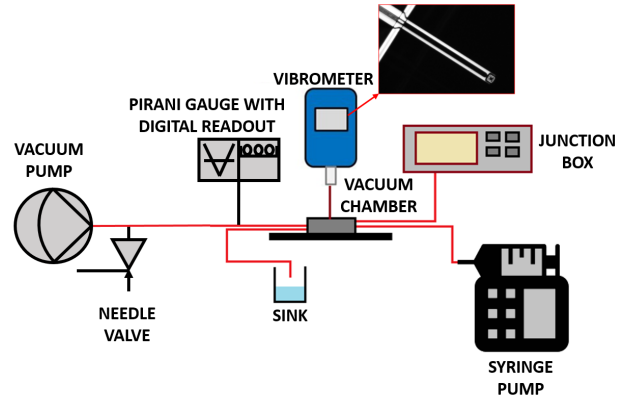


Figure 3: Components of the setup for the characterization of hollow cantilevers.

frequency resolution and consequently the ability of the device to detect small changes in density. Air damping is one of the main factors limiting the QF. To reduce air damping, the device along with the holder which provides the base excitation were placed inside a vacuum chamber. The connection between the chamber and the vacuum pump also accommodates a leak valve to control the vacuum level in the chamber and a Pirani gauge for vacuum level readout. Optical access for the measurement laser was provided by means of a glass window in the vacuum chamber. A built-in microscope on the vibrometer facilitates positioning of the laser at the desired position. Current position of the laser can be seen in Figure 3 (inset). The vacuum chamber also provides an interface for exchange of fluids by means of two needles glued on opposite faces of the chamber. Tygon tubings can be easily connected and disconnected from this chamber during experiments without affecting the vacuum level. The schematic of the setup with the various components can be seen in Figure 3.

3.2 Characterization

The experimental characterization of the hollow cantilever was performed using a laser doppler vibrometer (Polytec MSA-400-PM2-D). To ensure proper reflection of the laser from the transparent surface of silicon dioxide, the chip was coated with 6 nm of Au/Pd. The excitation was provided by a standard Atomic Force Microscope (AFM) holder (from Nanosurf) in the linear regime at different frequencies. This holder also ensures that the device can be reproducibly clamped in the same manner during multiple experiments. The resonance frequency and QF can then be extracted from the frequency-amplitude response. Determination of the QF obtained from the frequency-amplitude response was done by fitting a Lorentzian and then using the 3dB method on the Polytec Acquisition software. The fundamental frequency of this device, in air, is measured to be about 134 kHz, with a QF of

150. The second bending and the first torsional modes have also been obtained and their associated resonance frequency and QF are summarized in Table 2. The predicted values from simulation of the resonance frequencies (199.3 kHz, 1.24 MHz and 1.27 MHz) are higher than the obtained experimental values. The difference, to some extent, can be attributed to three main factors: the exact values of the Young's Modulus and Poisson ratio of the Silicon dioxide used in the fabrication are unknown. Second, the fabricated hollow cantilever, might be thinner or longer than designed. Third, the tip of the cantilever ends in a needle-like aperture, which adds mass to the cantilever (at the most sensitive position). We discount the effect of this mass in our simulations. The frequency vs amplitude response of the device (with 20 times averaging) in air while the measurement laser is focused at a single point on the hollow cantilever (close to the tip on one of the legs) can be seen in Figure 4. With increasing mode number, we observe an increase in the QF of the device.

Table 2: Resonance frequencies and Quality factors (in air).

Mode	Resonance freq	Quality factor
First bending	134 kHz	150
Second bending	828 kHz	320
First torsional	916 kHz	400

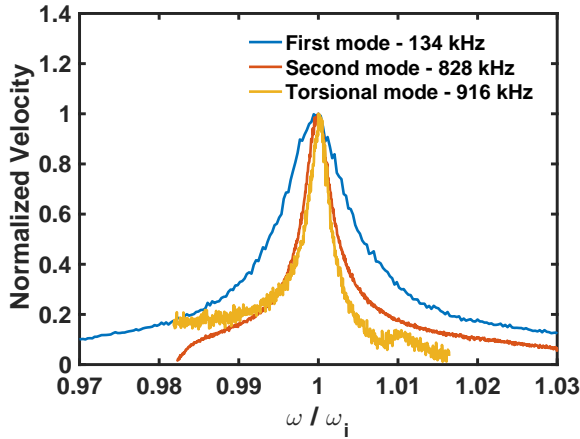


Figure 4: Resonant Modes of the empty device in air. Here ω_i refers to the resonance frequency of the specific mode.

As we approach medium vacuum levels in the chamber the resonance frequency of the device is found to increase. This increase is more prominent for the second mode where the increase in resonance frequency from air to 2.8 mbar is roughly 1.6 kHz (Figure 5b). This is consistent with the definition of the damped eigen frequency [14]:

$$\omega_d = \omega_n \sqrt{1 - 2\tau^2} \quad (1)$$

where ω_n is the natural frequency and τ is the damping ratio. As the vacuum level improves, the damping ratio reduces and the damped eigen frequency increases. However, the parameter of interest is the QF of the device. When the effect of air damping is lowered, at 2.8 mbar, the QF for the first bending mode improves to 1700 (≈ 10 times increase) and improves by roughly 20 times to 5200 and 8200 for the second bending and first torsional mode, respectively.

3.3 Density measurement using higher modes

Following the modal testing of the hollow cantilever in air and vacuum, the cantilever is filled with three different fluids of varying densities and viscosities. In hollow cantilevers, shifts in the inverse square of the resonance frequency are directly proportional to changes in fluid density. Mathematically, this can be expressed as [2]:

$$\rho_f = \left(\frac{A}{\omega_r} \right)^2 - B \quad (2)$$

The three fluids along with their viscosities and densities at 20°C have been tabulated in Table 3. All fluids are stored and supplied to the hollow cantilever at 20°C. All fluids were double filtered using 0.1 μm dis-

Table 3: Density and Viscosity of the characterized fluids at 20°C (Data obtained from MSDS).

Fluid	Density in kg/m^3	Viscosity in mPas
Water	1000	0.890
Ethanol	779	1.100
Ethylene Glycol	1110	16.200

posable filters, to eliminate particles (or agglomerates) that could clog the channels. Fresh tubings and syringes were used for every fluid. The fluids were flown through the hollow cantilever using a standard syringe pump with a flow rate of 5 $\mu\text{L}/\text{min}$. The complete exchange of fluids takes roughly 3-4 minutes. After the complete exchange of fluids, measurements were conducted after a time interval of 10 minutes to ensure that the experimental condition is stabilized. In the case of ethylene glycol, a second syringe pump withdrawing the fluid from the hollow cantilever at a rate of 5 $\mu\text{L}/\text{min}$ was used. This is because glycol is a more viscous liquid (≈ 16 times more viscous) compared to water and ethanol. Water was passed through the device before and after all ethanol/glycol related experiments.

4 Results and discussion

After the characterization of the empty hollow cantilevers (2.8 mbar vacuum) (Figure 6) we observed

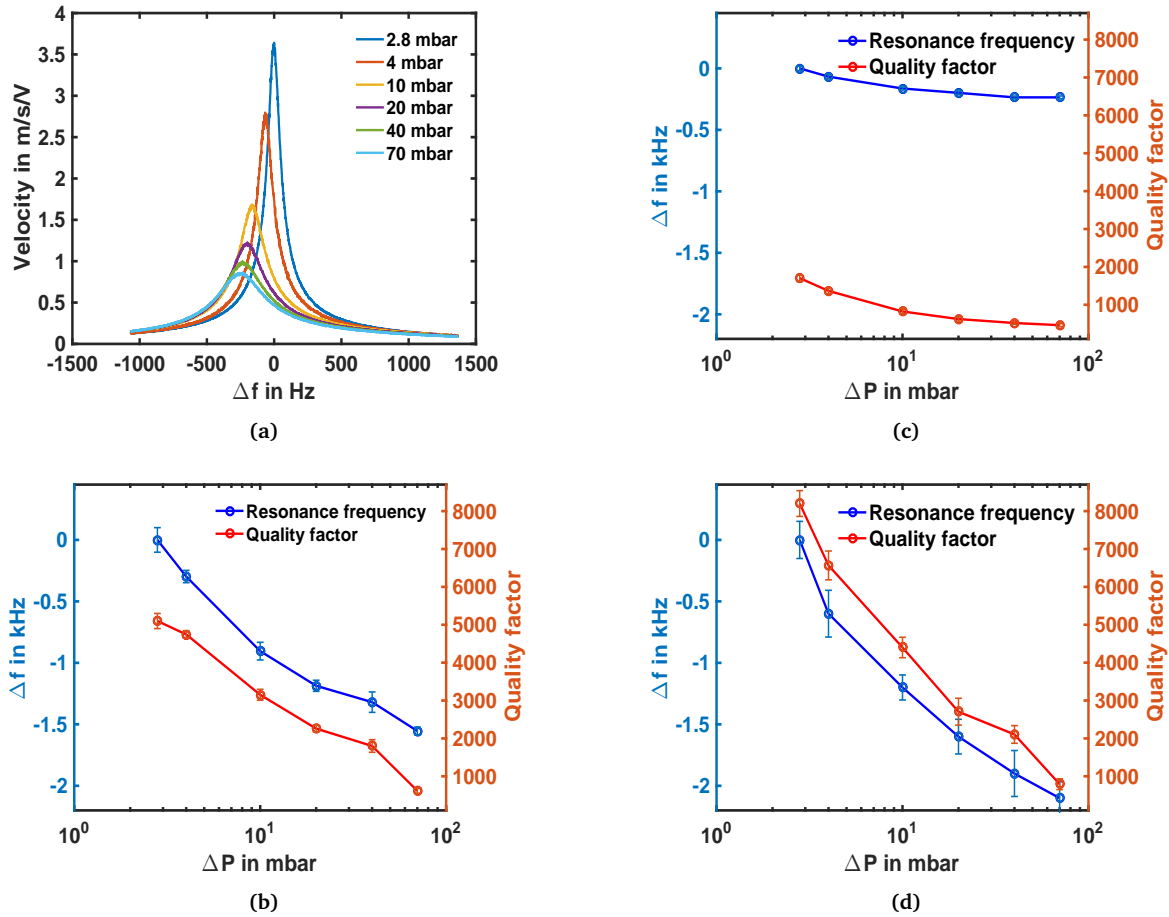


Figure 5: (a) Frequency shift observed for the first mode as pressure in the vacuum chamber is increased; (b) resonance frequency shifts (from 828.5 kHz) and QFs plotted as a function of the pressure in the chamber for the second bending mode; (c) resonance frequency shifts (from 134.5 kHz) and QFs plotted as a function of the pressure in the chamber for the first bending mode; (d) resonance frequency shifts (from 917 kHz) and QFs plotted as a function of the pressure in the chamber for the first torsional mode. (Note : All baseline values at 2.8 mbar)

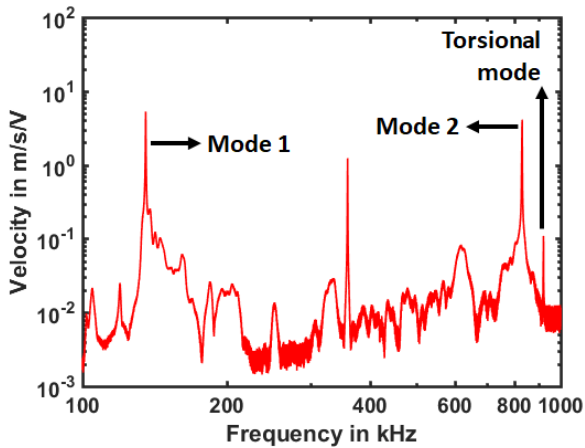


Figure 6: Amplitude-Frequency response of the hollow cantilever in vacuum on a log-log scale (Bandwidth of 900 kHz). The peak observed at 358 kHz is linked to the combination of the rigid body motion of the base and the first bending mode of the hollow cantilever.

that the improvement in QF is roughly of an order of magnitude (See Table 4). The QF of the first mode of our devices are approximately 15 times lower when compared to the QFs of the devices (for density and viscosity sensing) used in the work of Khan et al [2]. These devices operate at a pressure 10^5 times lower than the pressures attainable in our setup. The devices (for density and mass sensing) used by Manalis [15], possess 8 times higher QFs for the first mode in high vacuum. This is similar to the QF of the first torsional mode of our device.

Table 4: Comparison of QFs in air and at 2.8 mbar.

Mode	Quality factor in air	Quality factor at 2.8 mbar
First bending	150	1700
Second bending	320	5200
First torsional	400	8200

Repeated measurements with an interval of one minute of the resonance frequencies of empty hollow cantilevers were then carried out to characterize the short

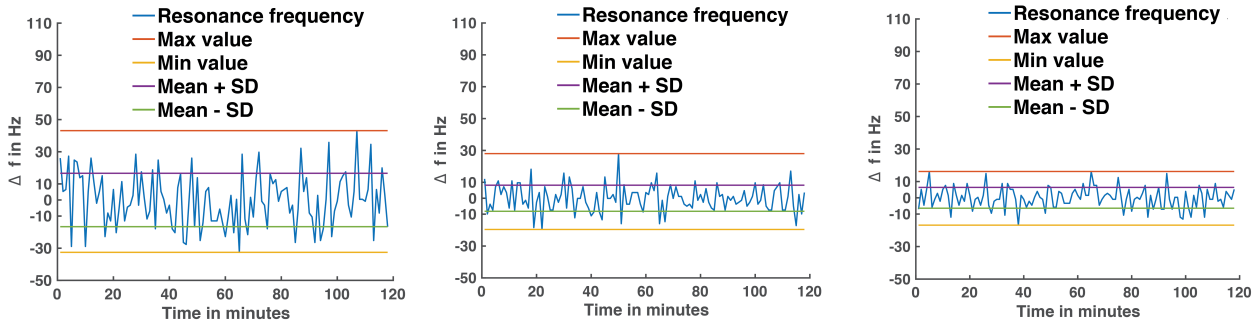


Figure 7: Resonant frequency measurement over two hours for the first (134.5 kHz), second bending (828.5 kHz) and first torsional mode (917 kHz) respectively (left to right). SD refers to standard deviation.

term frequency stability of the device in standard measurement conditions. We obtain the resonance frequencies from the measured frequency-amplitude/phase spectrum. The resonance frequencies are then plotted vs time for different modes (See Figure 7). We observe that for the first mode, the frequency varies between ± 16.6 Hz (one standard deviation) from the mean. Further, we observe that for the second mode and first torsional mode these values reduce to ± 8.2 Hz and ± 6.4 Hz respectively. This implies that at higher modes we can estimate the density better provided the sensitivity is not drastically reduced. It is important to note that we do not have any temperature control of our device (Temperature of laboratory is maintained at 20°C).

On filling the empty hollow cantilevers with fluids, we observe that the resonance frequency for all modes decreases as the density of the fluid in the channels increases. For one such experiment we plot the normalized amplitude responses and the phase vs frequency for the filling exercise (Figure 8 and 9). The chosen measurement point (close to the tip of the cantilever) in Figure 10 is not the optimal point for measuring the torsional mode of the device. The points closer to the tip and base are the points of minimum displacement in the torsional mode.

The resulting plots for resonance frequency (mean from all experiments) vs density show linear behaviour for the first mode (R^2 value = 0.9996 for the linear fit), second mode (R^2 value = 0.9994 for the linear fit) and the first torsional mode (R^2 value = 0.9998 for the linear fit)(Figure 11). From the slope of these plots we can obtain the sensitivity of our device. The sensitivity and previously mentioned resolution (for σ equivalent standard deviation) for all three modes have been tabulated in Table 5. It is evident that higher modes increase the sensitivity of our measurement with simultaneous improvement of the resolution. Further, the percentage change in density with respect to water that is measurable using the three modes can be found in Table 5. The percentage change in density that is detectable using the first torsional mode (.011%) is better than the density change of 0.06% that can be detected using Mode 17 of cantilevers immersed in

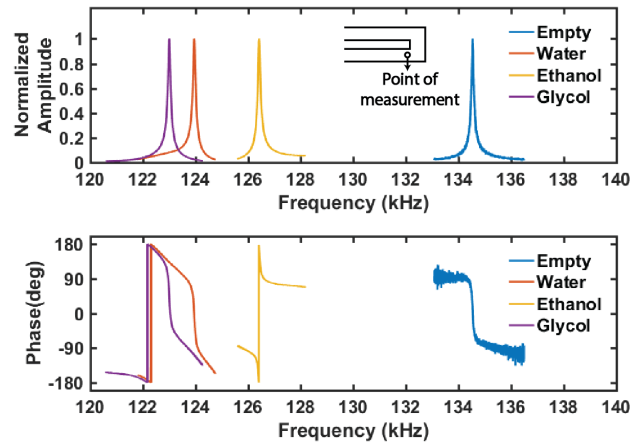


Figure 8: Resonant frequency shift of the first mode in the presence of different fluids.

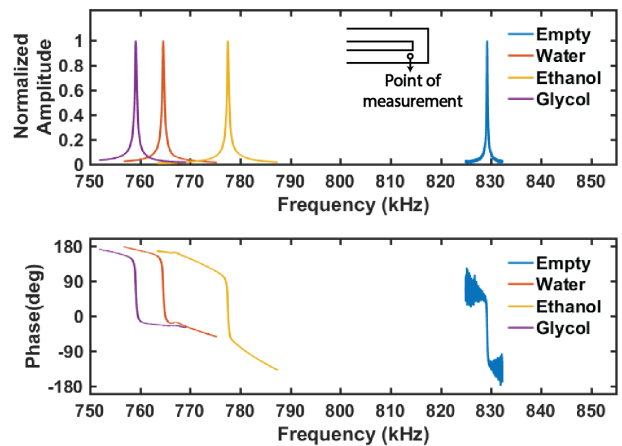


Figure 9: Resonant frequency shift of the second mode in the presence of different fluids.

fluids [16].

In Figure 8,9 and 10 we plot the normalized amplitudes (velocity in m/s/V) vs frequency. However, in our measurements the amplitude first drops from the empty scenario and then increases successively for ethanol,

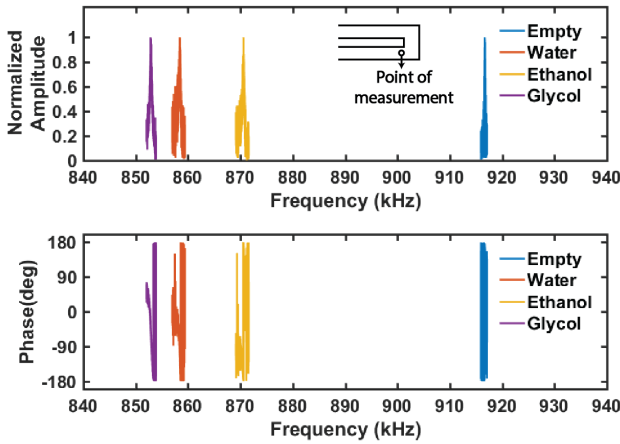


Figure 10: Resonant frequency shift of the first torsional mode in the presence of different fluids.

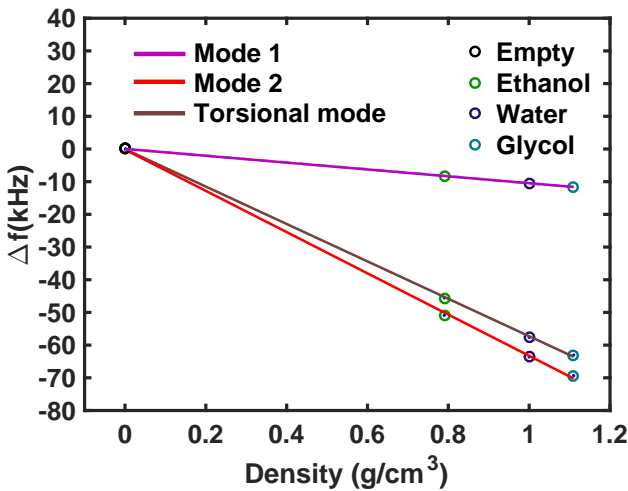


Figure 11: Resonant frequency shift of the three modes in the presence of different fluids. The reading of the empty cantilever is taken as the baseline reading for all three modes.

Table 5: Sensitivity and resolution of various modes.

Mode	Sensitivity Hz/kg/m ³	Resolution Hz(kg/m ³)	Detectable % change in density
First	10.49	16.6 (1.58)	0.158
Second	63.01	8.2 (0.13)	0.013
Torsional	57.16	6.4 (0.11)	0.011

water and glycol for the first bending mode and the first torsional mode. For the second bending mode, the amplitude first decreases from ethanol to water and then increases for glycol. A similar change of amplitude while filling the cantilever has previously been reported in [17]. We observe such a behavior for all three experiments which is another indication (apart from frequency shift) that the channels in the

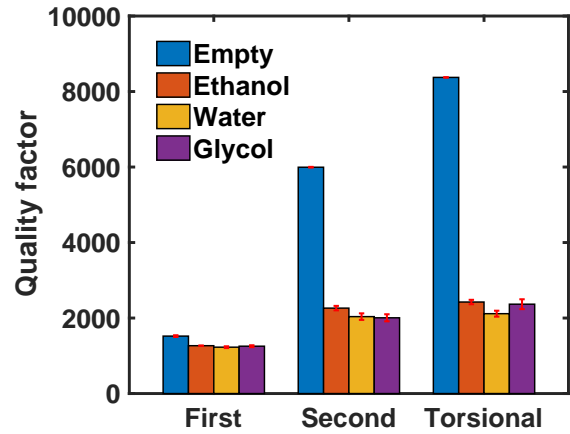


Figure 12: Quality factors for the first two bending and the first torsional mode when the hollow cantilever is filled with air (empty), ethanol, water and glycol.

device are occupied by the fluid. The amplitude of the response maybe important when a feedback loop is implemented, as higher amplitudes generate lesser frequency noise in feedback [18].

The QFs obtained for all the modes in the presence of fluids can be seen in Figure 12. It is clear that the empty hollow cantilevers have the highest QF for all modes, and the fluid filled hollow cantilevers are subject to a loss in QF. The QF almost remains the same irrespective of the fluid in the channels. If we take a closer look at the QF for the first mode between the different fluids: Ethanol(1267±2.5),Water(1228±23.8) and Glycol(1254±24). The relationship between QF and viscosity is non-monotonic with increasing viscosity, for the first bending and first torsional mode, as predicted in the theoretical and experimental works of Sader et al [19]. However, we are unable to confirm this because of a) limited experiments with fluids of varying viscosity and b) the measurement error in QF is comparable to the difference in QF of the fluids. In our devices the QF increases appreciably as mode number increases. This behavior cannot be predicted by the model [19] of hollow cantilevers, which instead predicts a drop in QF as mode number increases.

5 Conclusion

In this work, we present hollow cantilever devices that possess QFs of about 1700 for the first bending mode of vibration in 2.8 mbar vacuum. These QFs are found to increase as the mode number increases, which is unique to our devices because of its geometry. The first torsional mode exhibits a QF of about 8000, which is comparable to the QF of devices used in state-of-the-art cantilever based mass sensing applications. With these devices we measure the change in resonance frequency for two bending modes and one torsional mode while filling liquids in the channels. The respective density

sensitivities for the three modes are 10.49 Hz/kg/m³, 63.01 Hz/kg/m³ and 57.16 Hz/kg/m³. There is also an improvement in resolution from 1.58 kg/m³ to 0.11 kg/m³ as we approach higher modes of vibration which make the latter more attractive for sensing. This is done without the aid of complex frequency tracking systems. We envision that ultimately our devices when in higher vacuum and equipped with a frequency tracking system (in a feedback loop), can be used for high throughput mass sensing applications for both nano particles and biological media.

References

- [1] D. Sparks, S Massoud-Ansari, M. Straayer, R Smith, R Schneider, J Cripe, Y Zhang, and G Meng, "A density/specific gravity meter based on silicon microtube technology", Jan. 2002.
- [2] M. Khan, S. Schmid, P. Larsen, Z. Davis, W. Yan, E. Stenby, and A. Boisen, "Online measurement of mass density and viscosity of pl fluid samples with suspended microchannel resonator", *Sensors and Actuators B: Chemical*, vol. 185, pp. 456–461, 2013, ISSN: 0925-4005. DOI: <https://doi.org/10.1016/j.snb.2013.04.095>. [Online]. Available: <http://www.sciencedirect.com/science/article/pii/S0925400513005285>.
- [3] H. Fadaei, B. Scarff, and D. Sinton, "Rapid microfluidics-based measurement of co2 diffusivity in bitumen", *Energy & Fuels*, vol. 25, no. 10, pp. 4829–4835, 2011. DOI: 10.1021/ef2009265. eprint: <https://doi.org/10.1021/ef2009265>. [Online]. Available: <https://doi.org/10.1021/ef2009265>.
- [4] M. K. Ghatkesar, V. Barwich, T. Braun, J.-P. Ramseyer, C. Gerber, M. Hegner, H. P. Lang, U. Drechsler, and M. Despont, "Higher modes of vibration increase mass sensitivity in nanomechanical microcantilevers", *Nanotechnology*, vol. 18, no. 44, p. 445 502, 2007. [Online]. Available: <http://stacks.iop.org/0957-4484/18/i=44/a=445502>.
- [5] B. A. Bircher, L. Duempelmann, K. Renggli, H. P. Lang, C. Gerber, N. Bruns, and T. Braun, "Real-time viscosity and mass density sensors requiring microliter sample volume based on nanomechanical resonators", *Analytical Chemistry*, vol. 85, no. 18, pp. 8676–8683, 2013, PMID: 23905589. DOI: 10.1021/ac4014918. eprint: <https://doi.org/10.1021/ac4014918>. [Online]. Available: <https://doi.org/10.1021/ac4014918>.
- [6] P. Belardinelli, M. Ghatkesar, U. Staufer, and F. Alijani, "Linear and non-linear vibrations of fluid-filled hollow microcantilevers interacting with small particles", *International Journal of Non-Linear Mechanics*, vol. 93, no. Supplement C, pp. 30–40, 2017, ISSN: 0020-7462. DOI: <https://doi.org/10.1016/j.ijnonlinmec.2017.04.016>. [Online]. Available: <http://www.sciencedirect.com/science/article/pii/S002074621630364X>.
- [7] T. Braun, V. Barwich, M. K. Ghatkesar, A. H. Bredekamp, C. Gerber, M. Hegner, and H. P. Lang, "Micromechanical mass sensors for biomolecular detection in a physiological environment", *Phys. Rev. E*, vol. 72, p. 031 907, 3 2005. DOI: 10.1103/PhysRevE.72.031907. [Online]. Available: <https://link.aps.org/doi/10.1103/PhysRevE.72.031907>.
- [8] J. E. Sader, "Frequency response of cantilever beams immersed in viscous fluids with applications to the atomic force microscope", *Journal of Applied Physics*, vol. 84, no. 1, pp. 64–76, 1998. DOI: 10.1063/1.368002. eprint: <https://doi.org/10.1063/1.368002>. [Online]. Available: <https://doi.org/10.1063/1.368002>.
- [9] T. P. Burg and S. R. Manalis, "Suspended microchannel resonators for biomolecular detection", *Applied Physics Letters*, vol. 83, no. 13, pp. 2698–2700, 2003. DOI: 10.1063/1.1611625. eprint: <https://doi.org/10.1063/1.1611625>. [Online]. Available: <https://doi.org/10.1063/1.1611625>.
- [10] T. Burg, M. Godin, S. Knudsen, W. Shen, G. Carlson, J. Foster, K. Babcock, and S. Manalis, "Weighing of biomolecules, single cells and single nanoparticles in fluid", *Nature*, vol. 446, p. 1066, 2007. DOI: 10.1038/nature05741. eprint: <http://dx.doi.org/10.1038/nature05741>. [Online]. Available: <http://dx.doi.org/10.1038/nature05741>.
- [11] T. P. Burg, A. R. Mirza, N. Milovic, C. H. Tsau, G. A. Popescu, J. S. Foster, and S. R. Manalis, "Vacuum-packaged suspended microchannel resonant mass sensor for biomolecular detection", *Journal of Microelectromechanical Systems*, vol. 15, no. 6, pp. 1466–1476, 2006, ISSN: 1057-7157. DOI: 10.1109/JMEMS.2006.883568.
- [12] J. L. Arlett and M. L. Roukes, "Ultimate and practical limits of fluid-based mass detection with suspended microchannel resonators", *Journal of Applied Physics*, vol. 108, no. 8, p. 084 701, 2010. DOI: 10.1063/1.3475151. eprint: <https://doi.org/10.1063/1.3475151>. [Online]. Available: <https://doi.org/10.1063/1.3475151>.

- [13] T. Hug, T. Biss, N. de Rooij, and U. Staufer, “Generic fabrication technology for transparent and suspended microfluidic and nanofluidic channels”, *Proceedings of the 13th International Conference on Solid-State Sensors, Actuators and Microsystems*, vol. 2, 1191–1194, 2005.
- [14] J. Lardies and S. Gouttebroze, “Identification of modal parameters using the wavelet transform”, *International Journal of Mechanical Sciences*, vol. 44, no. 11, pp. 2263 –2283, 2002, ISSN: 0020-7403. DOI: [https://doi.org/10.1016/S0020-7403\(02\)00175-3](https://doi.org/10.1016/S0020-7403(02)00175-3). [Online]. Available: <http://www.sciencedirect.com/science/article/pii/S0020740302001753>.
- [15] J. Lee, W. Shen, K. Payer, T. P. Burg, and S. R. Manalis, “Toward attogram mass measurements in solution with suspended nanochannel resonators”, *Nano Letters*, vol. 10, no. 7, pp. 2537–2542, 2010, PMID: 20527897. DOI: 10.1021/nl101107u. eprint: <http://dx.doi.org/10.1021/nl101107u>. [Online]. Available: <http://dx.doi.org/10.1021/nl101107u>.
- [16] M. K. Ghatkesar, E. Rakhmatullina, H.-P. Lang, C. Gerber, M. Hegner, and T. Braun, “Multi-parameter microcantilever sensor for comprehensive characterization of newtonian fluids”, *Sensors and Actuators B: Chemical*, vol. 135, no. 1, pp. 133 –138, 2008, ISSN: 0925-4005. DOI: <https://doi.org/10.1016/j.snb.2008.08.012>. [Online]. Available: <http://www.sciencedirect.com/science/article/pii/S0925400508005522>.
- [17] S. A. Manzoor Bukhari, M. F. Khan, A. Goswami, R. McGee, and T. Thundat, “Thermomechanical analysis of picograms of polymers using a suspended microchannel cantilever”, *RSC Adv.*, vol. 7, pp. 8415–8420, 14 2017. DOI: 10.1039/C6RA25455A. [Online]. Available: <http://dx.doi.org/10.1039/C6RA25455A>.
- [18] S. Olcum, N. Cermak, S. Wasserman, S.K.Christine, H.Atsumi, K.R.Payer, W.Shen, J. Leel, A. Belcher, S.N.Bhatia, and S.R.Manalis, “Weighing nanoparticles in solution at the attogram scale”, *Proceedings of the National Academy of Sciences*, vol. 111, no. 4, pp. 1310–1315, 2014. DOI: 10.1073/pnas.1318602111. eprint: <http://www.pnas.org/content/111/4/1310.full.pdf>. [Online]. Available: <http://www.pnas.org/content/111/4/1310.abstract>.
- [19] J. Sader, J.Lee, and S.Manalis, “Energy dissipation in microfluidic beam resonators: Dependence on mode number”, vol. 108, no. 11, 2010. DOI: 10.1063/1.3514100. [Online]. Available: <http://www.ncbi.nlm.nih.gov/pmc/articles/PMC3013155/>.

3

Thermoelastic coupling effects on the natural frequencies

All the measurements and results presented in Chapter 2 have been achieved by measuring single points of the hollow cantilever. The location of the measurement spot is chosen with respect to the mode to be investigated, for e.g. a point close to the tip of the cantilever gives the largest frequency-amplitude spectrum for the first mode. For the second mode however as we move towards the base, we first encounter a node (where the amplitude will be drastically reduced) and then move to higher amplitudes before the amplitudes are reduced again. Finally for the torsional mode, in which the two legs are free to move in counterphase, the amplitudes are highest at the center of the legs and successively decrease as we move away from the center. As is evident the measured amplitude is directly linked to the mode shape of the hollow cantilever.

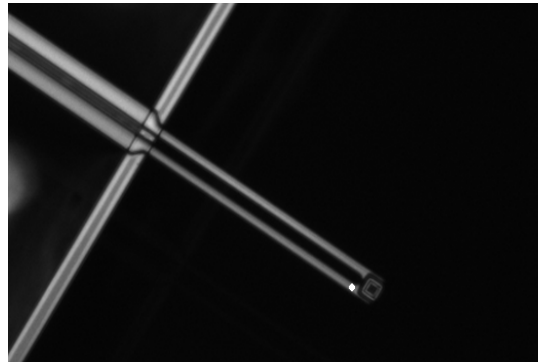


Figure 3.1: Position of laser chosen for single point measurements.

3.1. Mode shape imaging of hollow cantilevers

Building mode shapes is essential to determine which peaks in the frequency-amplitude/velocity response are effectively true modes of the hollow cantilever. Indeed, it is possible to incur in operating deflection shapes (ODS), shapes that are not eigenmodes of the system. For instance, shapes which are related to the combination of the modes of the hollow cantilever and rigid body modes of the chip and the actuation or clamping may be confused with the solution of the free unforced vibration problem if not correctly identified. Such peaks can be disentangled if mode shape imaging is performed. This is one of the advantages of using a laser doppler vibrometer (Polytec MSA 400) that allows for scanning the device geometry. Using the amplitude response at all the points in a given frequency range near resonance, the mode shapes can be built.

3.1.1. Mode shapes of hollow cantilevers in air

The first step was to use the setup designed to build the mode shapes of hollow cantilevers in air. We choose to analyze the response in a 1 MHz bandwidth, because the first two bending modes and the first torsional mode of our cantilevers are all below 1 MHz. The third flexural mode remains undetected since it is both beyond the maximum bandwidth of the Polytec and in the range where the power of the piezo excitation is reduced. The mode shapes of the first-two flexural modes and the first torsional mode are shown in Figures 3.2 - 3.4 respectively.

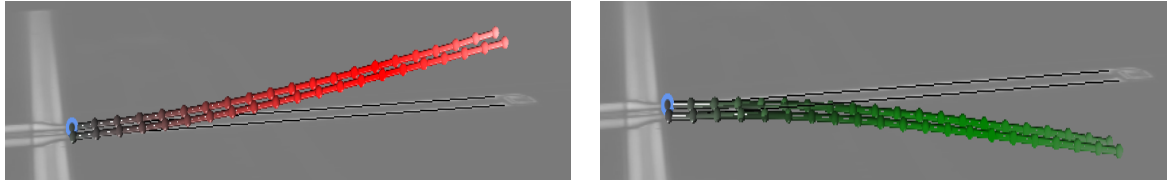


Figure 3.2: First bending mode of the hollow cantilevers in air (134.5 kHz). The two images represent the two extremities of motion in this particular mode shape.

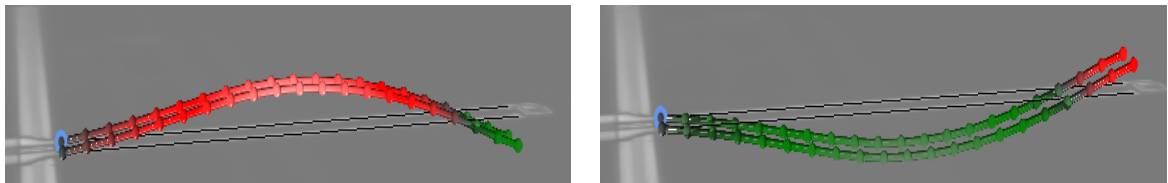


Figure 3.3: Second bending mode of the hollow cantilevers in air (828 kHz). The two images represent the two extremities of motion in this particular mode shape.

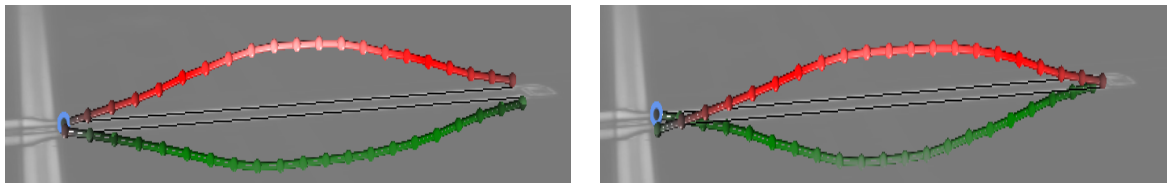


Figure 3.4: First torsional mode of the hollow cantilevers in air (916 kHz). The two images represent the two extremities of motion in this particular mode shape.

It is worth to observe that in the case of the torsional mode the motion sees the two legs moving in counter phase. Each of these mode shapes is linked to a peak in the average spectrum (which is essentially the sum of the responses at each data point divided by the number of data points). This is evident in Figures 3.5-3.7 that report the frequency-amplitude (velocity) peaks for the mode shapes under analysis. This also means that the resonance peak measured at each point on the cantilever is roughly the same for all modes. Indeed, linear eigenmodes describe the synchronous motion of all the points of the structure and only the oscillation amplitude (consequently the constitutive shape) varies along the cantilever. Such a behavior is consistent with our understanding of how mode shapes are built.

3.1.2. Mode shapes of hollow cantilevers in vacuum

We employ the same technique as we did for imaging mode shapes in air, to obtain the mode shapes in vacuum. A vacuum pump connected to the chamber enables us to create a rough vacuum of 2.8 mbar (Chapter 2). We then scan the hollow cantilever at multiple points to obtain an average spectrum (similar to the case in subsection 3.1.1). In a vacuum environment the operation of building mode shapes as done in air has not revealed to be as straightforward as in air for both the second bending mode and the first torsional mode. Also, the first mode shape has some elements moving out of phase with the motion.

If we closely inspect the average spectrums in vacuum, for the first mode we see a distinct peak, but for the other two modes we see multiple peaks stacked adjacent to each other. Building the mode shapes around any of these frequencies results in haphazard movement descriptions (mode shapes) of the hollow cantilever.

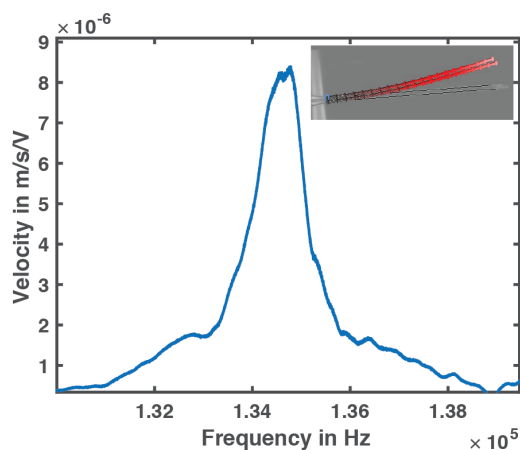


Figure 3.5: Mode shape linked to the peak in average spectrum of the hollow cantilevers in air (134.5 kHz). In the inset the mode shape associated with the first flexural resonant peak is shown.

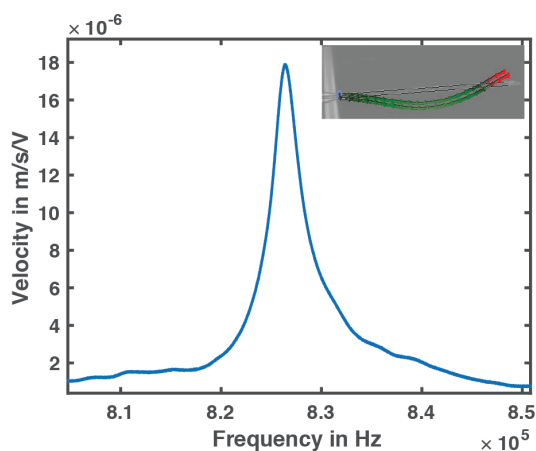


Figure 3.6: Mode shape linked to the peak in average spectrum of the hollow cantilevers in air (828 kHz). In the inset the mode shape associated with the second flexural resonant peak is shown.

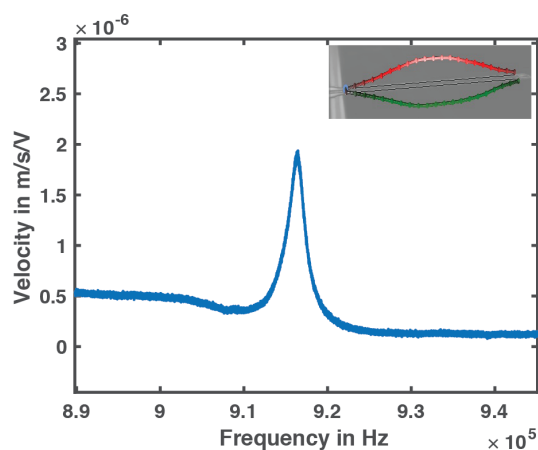


Figure 3.7: Mode shape linked to the peak in average spectrum of the hollow cantilevers in air (916 kHz). In the inset the mode shape associated with the first torsional resonant peak is shown.

We first eliminate the proposition that the vibrations of the vacuum pump or the setup itself are causing this multiple peak effect. We test standard contact mode Atomic Force Microscope (AFM) cantilevers on our setup in vacuum. The mode shapes and corresponding peaks in the average spectrum can be found in Appendix

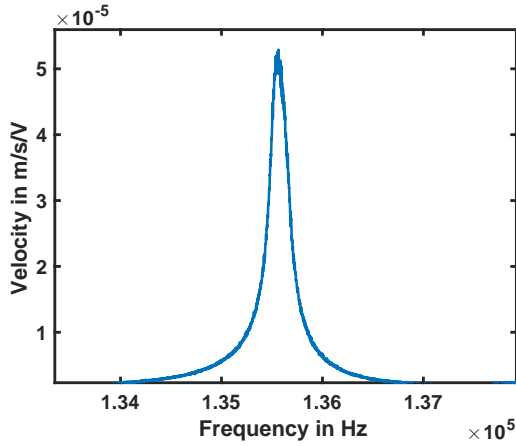


Figure 3.8: Average spectrum zoomed in at Mode 1 in vacuum.

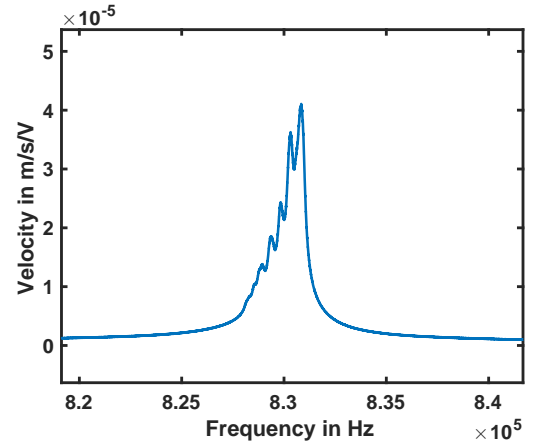


Figure 3.9: Average spectrum zoomed in at Mode 2 in vacuum.

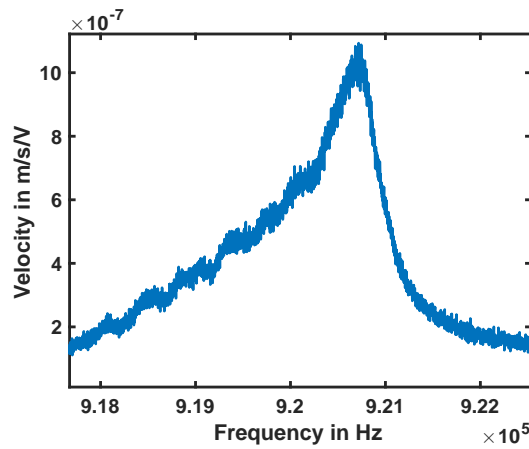


Figure 3.10: Average spectrum zoomed in at Mode 3 in vacuum.

E Given that we are able to build mode shapes of the AFM cantilevers in vacuum we turn our focus to the hollow cantilever itself.

3.2. Resonant frequency shift as a function of point location.

The average spectrum plots considered in subsection 3.1.1 are related to the single point measurements on a grid that we build on the hollow cantilever. A closer look at the measurement data at each of these points gives us insights of the effects that we see in the average spectrum. We plot the data obtained from the velocity - frequency response as we sequentially change the measurement laser position from the base of the cantilever up to the free end of the cantilever. Figure 3.11 shows the shift of the resonant peak for the first flexural resonance frequency, Figure 3.12 shows the variation around the second flexural resonance frequency and, lastly, the variation around the torsional mode resonance frequency is reported in Figure 3.13. The data is plotted for one leg of the hollow cantilever. The observed trend in the other leg of the hollow cantilever is similar, but the exact values do not match because we cannot precisely locate the point on the other leg manually with the accuracies that are required.

As expected, in all the cases the shape of the mode modulates the intensity of the response. However Figures 3.11 - 3.13 also highlight the variation of the resonant frequency as the laser moves from the base to the cantilever tip.

In order to have a better visualization of the change in frequency, the relative frequency shift percentages with respect to the measured resonance frequency values at the point closest to the tip, can be seen in Figure

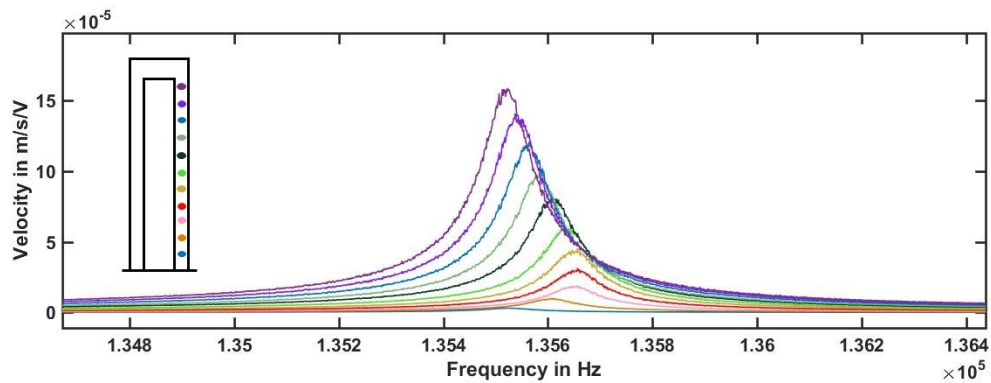


Figure 3.11: Frequency - Amplitude response of multiple points on one leg of the hollow cantilever at the first bending resonance frequency. Colour of the plots correspond to the colour of the dots on the hollow cantilever (inset).

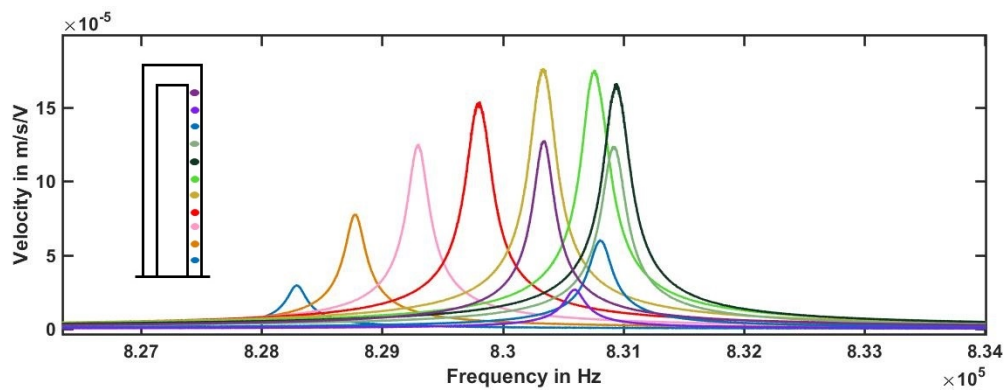


Figure 3.12: Frequency - Amplitude response of multiple points on one leg of the hollow cantilever at the second bending resonance frequency. Colour of the plots correspond to the colour of the dots on the hollow cantilever (inset).

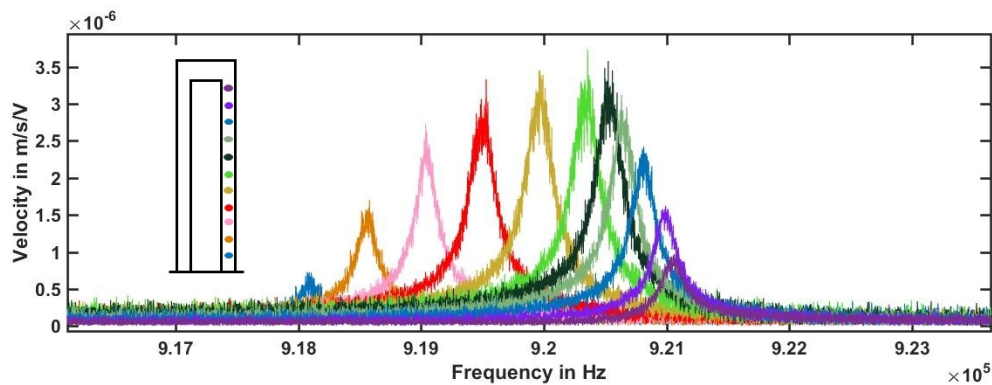


Figure 3.13: Frequency - Amplitude response of multiple points on one leg of the hollow cantilever at the first torsional resonance frequency. Colour of the plots correspond to the colour of the dots on the hollow cantilever (inset).

3.14. We observe that the shifts are clearly mode dependent. For the first bending mode the frequency first increases and then decreases as we move from the base to the tip. For the second bending mode, the frequency continuously increases and after reaching a maximum decreases. Finally, for the first torsional mode we see observe a continuous increase in the resonance frequency as we move from the base to the tip.

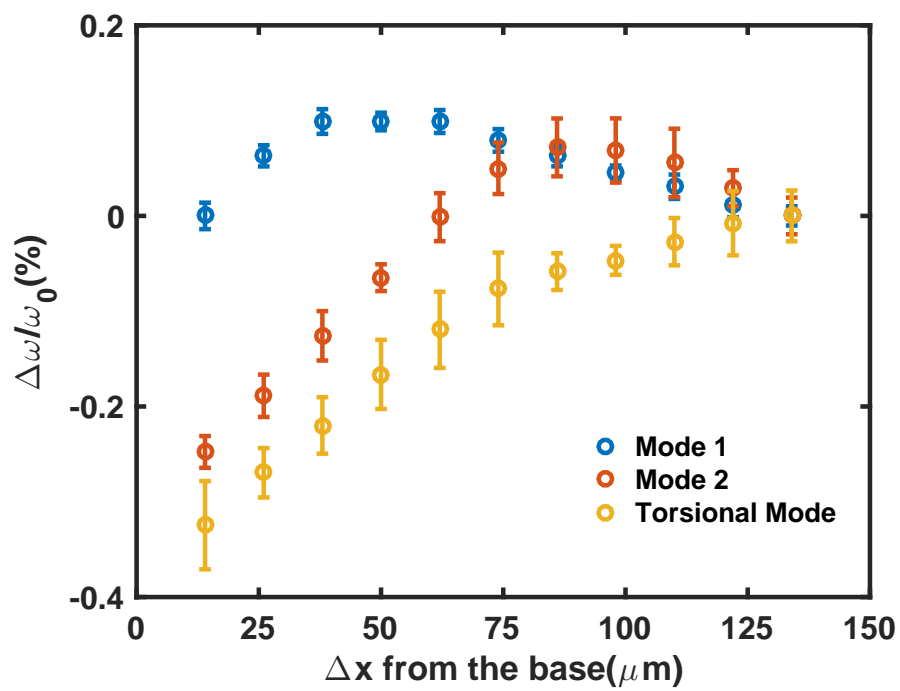


Figure 3.14: Experimental percentage relative frequency shift for mode 1, mode 2 and the torsional mode as we move away from the base of the cantilever (from left to right). Error bars show standard deviation over three different hollow cantilevers. The reference frequency is assumed to be the frequency at the point closest to the tip of the cantilever.

3.3. Measurement laser-induced frequency shift

The detection of the resonance frequency of micro- and nano-resonators is usually done by an optical based detection method [33–35]. Since most of the identification techniques for added material are based on the induced frequency shift, the stability of the baseline resonant frequency is a vital requirement and only then the frequency shift due to the mass can be detected accurately [36, 37]. In order to detect the frequency shift with as high a resolution as possible, it is necessary to improve the signal to noise ratio. This is usually done by increasing the probing power of the measurement laser [38].

The measurement laser, if at high enough power, has been found to heat up the device [39]. Furthermore, this assumes particular importance if the measurements are done in vacuum, since the most efficient path for the heat to escape is through the microbeam cross section by conduction. This is in contrast to air where the surrounding air molecules can assist in heat transfer away from the cantilever by convection. The heating of micro cantilevers induced by the measurement laser and the subsequent shift in resonance frequency has been discussed in [37, 40]. This phenomenon is in accordance with the experimental findings and explains the problem we encounter with building mode shapes and the movement of resonance frequency we observe when we scan across the length of the cantilever in vacuum.

As we increase the laser power in a single point measurement we observe an increase in the resonance frequency of hollow cantilevers (Appendix G). This trend is opposite to the effect observed in silicon cantilevers without hollow channels [37] and primarily related to the variation of the stiffness induced by the thermoelastic coupling. The stiffness of cantilevers without hollow channels can be written as:

$$k = \frac{3EI}{l^3} \quad (3.1)$$

where E is the Young's modulus, I is the moment of inertia and l is the length of the cantilever. As the temperature coefficient of E (for Silicon) is negative, when the temperature increases the cantilever will soften. This results in a reduction in the resonance frequency of the cantilever. In the case of our devices we make use of Silicon dioxide, which is reported to have a positive temperature coefficient of Young's Modulus [41]. Hence, if the Young's modulus increases with temperature (with increasing laser power) the stiffness will increase. Localized heating may also increase the values of the height and breadth of the cantilever. These two contributing effects increase the stiffness, thereby increasing the resonance frequency when the laser power is increased.

If the laser power is increasing the temperature of the beam, it is important to estimate this temperature change. In some applications involving SMRs it maybe important to limit this increase in temperature to minimum levels so as to be able to work with biological media [42]. In the scope of this project however, heating of the cantilever is not significant. Density and viscosity of the fluid may vary slightly with temperature, as the fluid provides another path of heat transfer away from the laser spot. We assume the subsequent temperature drop in the hollow cantilever to be same for various fluids.

We estimate the temperature of the cantilever in vacuum using COMSOL, with the heating effect of the laser. In order to use a laser power value for the simulations, we measure the power of the laser with a laser power meter. The measured value at the focus is $200 \mu\text{W}$, after the laser has passed through the glass on the vacuum chamber. In the simulations we assume that all of the laser light is absorbed by the cantilever. However in reality the laser light has to be reflected to make detection possible. The temperature estimated is hence the maximum temperature expected and in reality the temperature values are below these values. We estimate the temperature values, for four different laser positions in Figures 3.15-3.18. As expected, the maximum heating of the cantilever occurs when the laser spot is positioned close to the tip, because conduction to the base is the most prominent heat transfer mechanism when the hollow cantilever is operated in vacuum. As we move closer to the base the heating reduces because now the chip is closer to the laser point and hence can take heat away from the cantilever more readily. It is evident that the heating effect due to the laser spot results in the asymmetric heating of the two legs of the cantilever. Finally, we estimate the change in the resonance frequency of the hollow cantilever due to the laser heating. In order to make a meaningful comparison, we simulate the heating effect at about the same points as we have performed the measurements in Figure 3.14. For the same laser positions, we simulate the frequency shift expected for the first and second bending modes

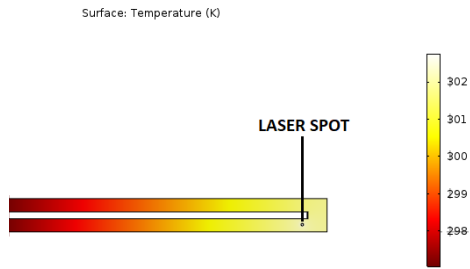


Figure 3.15: Temperature distribution with laser spot close to the tip of the leg.

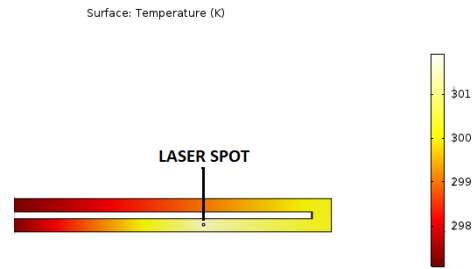


Figure 3.16: Temperature distribution with laser spot close to the center.

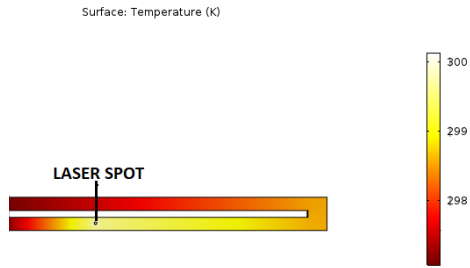


Figure 3.17: Temperature distribution with laser spot about halfway between the center and the base.

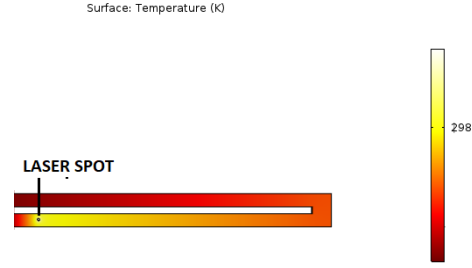


Figure 3.18: Temperature distribution with laser spot close to the base.

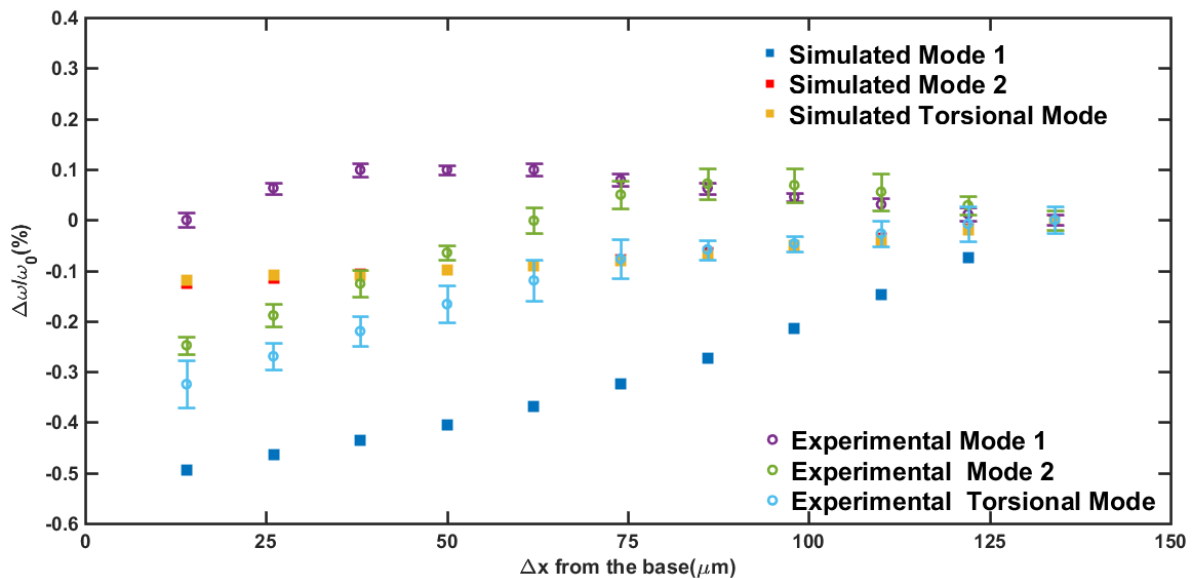


Figure 3.19: Simulated vs experimental percentage relative frequency shift for mode 1, mode 2 and the torsional mode as we move away from the base of the cantilever (from left to right). Error bars show standard deviation over three different hollow cantilevers. The reference frequency is assumed to be the frequency at the point closest to the tip of the cantilever.

and the first torsional mode in Figure 3.19. In the same figure the measured values are also plotted (with error bars). The simulations show a decrease in frequency for all the modes in consideration. This is consistent with the temperature distribution simulation. As the highest temperature achieved reduces as we move towards the base, the resonance frequency also keeps reducing as we move towards the base. The torsional mode in the experiments exhibits the same behavior (trend) as we scan from the tip towards the base on one leg of the cantilever. However the initial increase and subsequent decrease in frequency observed in the first bending mode and the increase in frequency till the laser reaches roughly the position of the node in the second bending mode may be attributed to slight variations in the cantilever fabrication which cannot be

accounted for in the simulation. Additionally, we have not measured the exact temperatures on our hollow cantilevers experimentally. It might be possible that the temperature deviations in practice are more than what we expect from simulations, and hence can have a more pronounced effect on the local geometry of the beam. Lastly, it might be worth to consider the temperature dependence of E since the value of the Young's modulus must change with temperature (which also means it must change as a function of position in hollow cantilevers), since this has not been modelled in our simulations.

4

Conclusion

This research has greatly enhanced our understanding of hollow cantilevers (fabricated at TU-Delft). Experimental characterization of the resonance frequencies and quality factors of the devices in both air and vacuum, clearly show the advantages of performing experiments at better vacuum levels. This advantage is primarily because of the improvement in quality factor at better vacuum levels. The resonance frequency shifts and change in quality factor when the channels of the hollow cantilevers were filled with fluids of varying densities/viscosities were investigated. Furthermore, the thermoelastic coupling effects of the measurement laser on the natural frequencies were studied. This study made it evident that as the frequency shifts that we want to detect become smaller (usually the case for nanoparticles or biological species), the ambient pressure and temperature of the hollow cantilever must be as stable as possible. This would reduce the likelihood of frequency shifts being caused by factors other than the fluid/particle of interest.

The answers to the two research questions are clear:

'What is the improvement in resolution and sensitivity (if any) when higher modes are used for the determination of density?'

The fundamental mode of vibration has a density sensitivity of 10.49 Hz/kg/m^3 . In comparison, the density sensitivity is 57.16 Hz/kg/m^3 for the first torsional mode and 63.01 Hz/kg/m^3 for the second bending mode. Thus it is evident that higher modes of vibration increase the sensitivity of density determination. The minimum change in density (resolution) that can be determined by monitoring the fundamental mode of vibration is 1.58 kg/m^3 . The resolution improves to 0.13 kg/m^3 for the second bending mode and 0.11 kg/m^3 for the first torsional mode. It can be concluded that by monitoring higher modes of vibration the improvement in sensitivity is about six times with a simultaneous improvement in resolution (fifteen times).

'What is the smallest density change that can be experimentally determined using hollow cantilevers fabricated at TU-Delft?'

By monitoring the first torsional mode of the hollow cantilevers, the smallest density change that can be detected is 0.11 kg/m^3 . This corresponds to being able to detect a 0.011 % change in the density of water. This value is six times better than the density change of 0.06 % that can be detected using Mode 17 of cantilevers immersed in fluids [30]. However, in state of the art density sensing using hollow cantilevers, the cantilevers are able to detect a 0.01 % change in density of water [27]. This can be mainly attributed to the higher quality factors obtained when the vacuum pressure is lower than 10^{-5} mbar.

It is possible to further improve the resolution and even sense smaller changes in density using hollow cantilevers. Some recommendations on how future research could be directed to achieve better resolutions can be found in the following chapter.

5

Recommendations

During the course of this project, it became apparent that improvements are possible on many fronts, in order to fully realize the potential of hollow cantilevers. Besides the improvements, several recommendations to reduce experimental uncertainties in future research are listed below:

- **Improving vacuum levels in the chamber.**

In the current experimental setup the vacuum limit is mainly imposed by the vacuum pump (0.5 mbar). By switching to a pump capable of evacuating the chamber to 10^{-3} mbar - 10^{-5} mbar, the quality factor is expected to increase. From the quality factor vs pressure plot in Chapter 2 it is evident that our system is in the region of momentum damping where individual air molecules are colliding and exchanging momentum with the resonator at a rate proportional to their difference in velocity [43]. At sufficiently low pressures the damping will only be due to the resonator and the quality factor will saturate to the intrinsic quality factor [44]. It is desirable to achieve quality factors as close to the intrinsic quality factor as possible. Since our chamber uses o-rings for sealing, we expect the chamber to be capable of handling high vacuum levels. The materials used for height compensation (Appendix A) need to be fabricated again, as 3-D printed parts may outgas at high vacuum levels.

- **Tracking the resonance frequency of the hollow cantilever.**

Measuring the frequency amplitude response of the device successively is not the optimal way to determine frequency shifts. In such a situation there is a large time interval between two consecutive determinations of the natural frequency. It is very likely that we lose a lot of information in this time. In most applications, either a phased locked loop (PLL) or self sustained oscillator allows for direct estimation of the natural frequency [31]. Resonance frequencies of multiple modes can be tracked with multiple PLLs. The multiple PLL method has been used to determine both mass and position of the particle simultaneously [45].

- **Understanding the effect of fluid viscosity on quality factor.**

In the case of hollow cantilevers the relationship between quality factor and fluid viscosity is non monotonic. In order to fully understand this effect for the devices, it is necessary to test with a large number of fluids with slightly different viscosities. Such an experiment would enable us to build a curve with sufficient data points. Additionally, if these experiments are done at better vacuum levels, it is likely that the differences between quality factors for different fluids is significant and greater than the measurement error. Understanding this behavior would enable viscosity measurements with hollow cantilevers.

- **Studying the effect of density on viscosity measurements.**

The quality factor can be calculated as the ratio of the resonance frequency to the full width of the resonance peak at half maximum. This means, that the density of the fluid can effect the quality factor measurement (which is linked to the viscosity) unless the effect of density on the QF is not significant. If the quality factor with fluids of similar viscosity but different densities are compared, it is possible to determine whether the density has an effect on the quality factor.

- **Reducing measurement laser power.**

High laser powers improve the signal to noise ratio (SNR) of the measurement and are hence desirable. However the measurement laser is found to induce thermoelastic coupling effects in the hollow

cantilever devices. It may be worth to reduce the laser power using optical attenuators in an effort to minimize the optical back action. This will be helpful in both mode shape imaging of the cantilevers in vacuum and while working with biological media.

- **Determining density sensitivity without empty cantilever reading.**

In vacuum, the heat generated by the measurement laser predominantly leaves the cantilever by means of conduction through the legs. However, when the channels are filled with fluid, some of the heat is taken away by the fluid in the channels. Hence, there is a resonance frequency shift not only because of the fluid density but also due to the temperature decrease. Thus, determining the density sensitivity only with the channels filled with multiple fluids could be an option to eliminate the effects of the measurement laser.

- **Thoroughly investigating the thermoelastic effects on the natural frequency.**

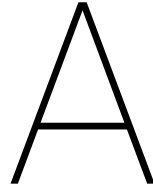
The current understanding of the effect of the measurement laser on the natural frequencies is limited. To obtain a clear understanding of the phenomenon, more experiments when the hollow cantilever is empty and filled with fluids in vacuum need to be conducted. The laser power can also be varied during these experiments. Modelling and simulations that can explain these effects at a more fundamental level could be valuable for future designs of hollow cantilevers.

- **Monitoring the temperature of the device.**

The effect of temperature on the resonance frequency of the device is apparent. Continuous monitoring of the temperature of the device would reduce the experimental uncertainty as then the resonance frequency shifts could be monitored either at the same temperature or the temperature effect could be accounted for.

- **Enabling higher actuation levels.**

In order to investigate the viability of using non linear phenomenon of softening or hardening for mass sensing, it is necessary to increase the excitation provided. The current setup is limited by the voltage that can be supplied to the piezo actuator in the AFM holder. Further testing with the existing holder at higher voltages or using a different piezo actuator can help overcome this limitation. Even if non linearity is not desired, higher amplitudes of response which are a result of higher excitation can help reduce the noise in the feedback loop [12].



Setup fabrication

In order to characterize the hollow cantilevers it is primarily necessary to have the clamping, actuation and measurement systems in place. Additionally, since we perform our experiments in vacuum and with fluids in the channels of the cantilever, it is important to integrate the vacuum and fluidic related elements seamlessly into one setup. This appendix discusses all the topics listed above, with the exception of the measurement system, which is discussed in Chapter 1.

A.1. Vacuum compatible chamber

Table A.1: List of parts of vacuum chamber.

Item No	Part Name
1	Base of vacuum chamber
2	O-Ring
3	Lid of vacuum chamber
4	Microscope slide
5	Socket head cap screw M4 X 6

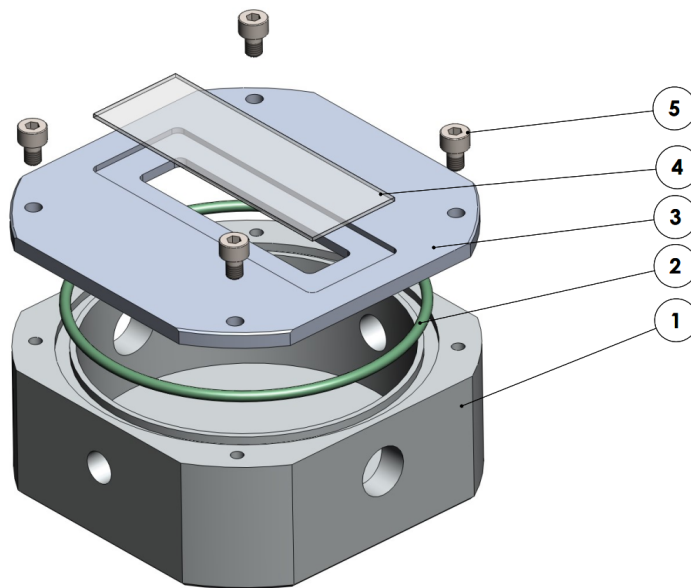


Figure A.1: Isometric view of the basic components of the vacuum chamber.

Because of its relative ease of machinability and low out-gassing unanodized-Aluminum is the material chosen for the chamber and the components to be attached to this base chamber (for instance the fluidic connections). The base of the chamber (part 1 in Figure A.1) is sealed by an o-ring (part 2) which is placed between the base and the lid (part 3). A microscopic slide, 1mm thick (part 4), is glued to the top of the lid, in order to provide optical access for the measurement. Finally, the base and the lid are completely attached together by fastening with four symmetrically located cap screws (part 5).

Table A.2: List of added parts of vacuum chamber.

Item No	Part Name
1	SMA connector with O -ring
2	Fluidic connection
3	General purpose dispense tips
4	O-Ring
5	Body and lid of vacuum chamber
6	Pneumatic threaded to tube adapter

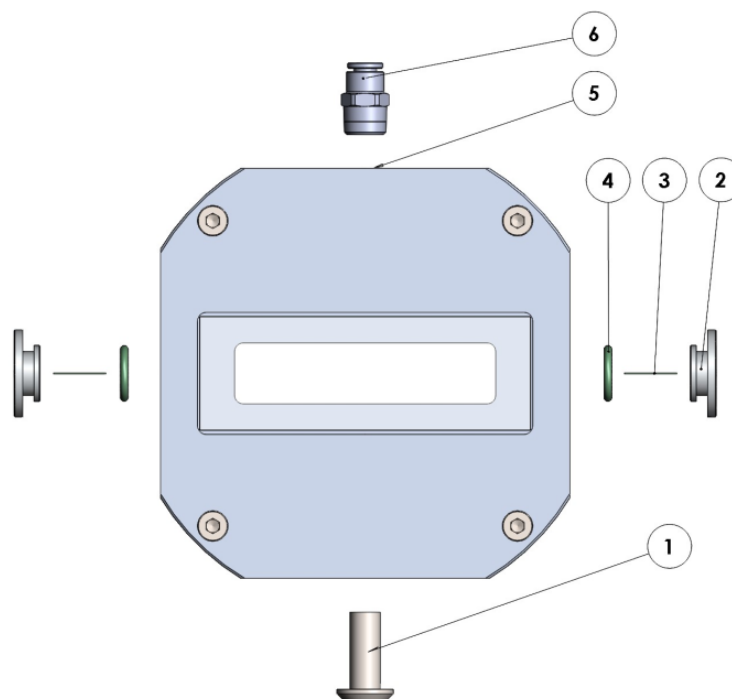


Figure A.2: Top view of the fluidic, electrical and vacuum attachments of the vacuum chamber.

The four holes in the base of the vacuum chamber are intended for electrical, fluidic and vacuum connections. The electrical connector (part 1 in Figure A.2) is a vacuum compatible (with an o-ring) SMA connector with solder termination inside the chamber. The fluidic connectors are composed of three main parts: a part which houses (part 2) the needle and the o-ring and fits into the chamber directly. The precision dispense tips (part 3) are glued through a small hole inside the housing. Thus the fluidic connector is capable of providing connections for the tygon tubing on either side. Finally, an o-ring (part 4) is placed around the fluidic connector to make it vacuum tight. These two fluidic connectors (inlet and outlet) are placed diametrically opposite to each other and in line of the tubings on the hollow cantilever. The last hole in the chamber (part 5) is fitted with a pneumatic threaded to tube adapter (part 6). The threads lock with the corresponding threaded hole on the chamber. Teflon tape in between the threads aids the sealing of the chamber. The chamber is finally capable of creating a vacuum, once the two fluidic connectors are connected to the hollow cantilever (which

is inside the chamber) on either side.

A.2. Actuation

A standard AFM holder (from Nanosurf) can provide both the base excitation and the clamping for the hollow cantilever. The excitation is provided by an embedded piezo in the holder and the clamping is provided by a clip that can be placed on the cantilever. The cantilever needs to be placed in the groove under the clip (Figure A.3). The cantilever is smaller than the dimensions of the groove, which makes the positioning of the cantilever in the groove difficult. The cantilever positioning and clamping is made as reproducible as possible by gluing the cantilever to the fluidic interface (Appendix B). The fluidic interface is produced to fit the groove perfectly. The connections to the piezo have been made internally on the holder. The external voltage has to be provided via the electrical contacts on the back side (Figure A.3).

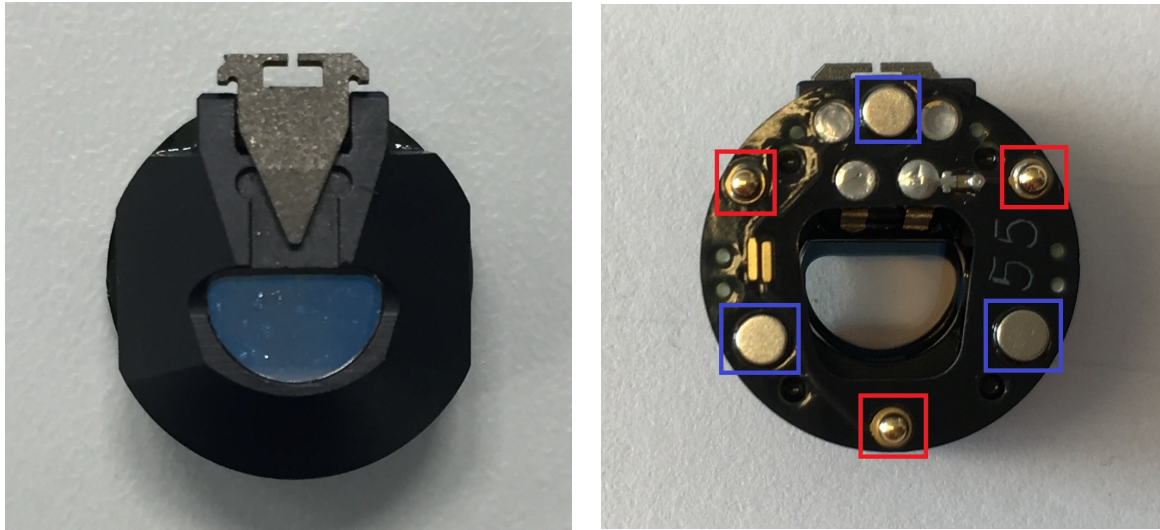


Figure A.3: Top and bottom view of the AFM cantilever holder. In the bottom view the blue squares denote magnetic connections and the red squares denote electrical connections.

The AFM holder has three magnets (marked by the blue squares in Figure A.3) and three electrical contacts (marked by the red squares in Figure A.3). These six components are particularly important in maintaining proper contact with the flexible printed circuit (FPC) (Figure A.4).

The three circular magnets on the AFM holder perfectly align with the three circular magnets on the FPC. Simultaneously, the three electrical contact balls on the holder make contact with the three v-grooves on the FPC. The three contacts are connected to three of the six pad ends on the FPC. The pad ends marked in red in Figure A.4 (b) are connected to the piezo, while the pad denoted with the black arrow is for the tip excitation. The AC voltage needs to be applied across the two pads marked in red. To avoid soldering on the FPC, the FPC is connected with a zero insertion force type FPC/FFC (flexible flat cable) to pin connector. The pins that correspond to the pads marked in red are soldered to two wires. One of these wires is also soldered at the other end to the SMA connector (which has a solder compatible termination) in the chamber. The other wire originating from the pin is grounded inside the chamber. The chamber is at ground since the outer portion of the SMA connection from the Polytec vibrometer is connected to the chamber. The circuitry is not isolated because the experiments are conducted in air and vacuum.

A.3. Height compensation

In the construction of the setup we have addressed the clamping and actuation of the hollow cantilevers. Additionally, the setup is equipped with fluidic connections and a port for the vacuum tube inlet. The final step is to ensure that the cantilever is within the working distance of the objective to be used for vibration measurements. At 20 times magnification, the working distance of the objective is approximately 20 mm (Polytec MSA datasheet).

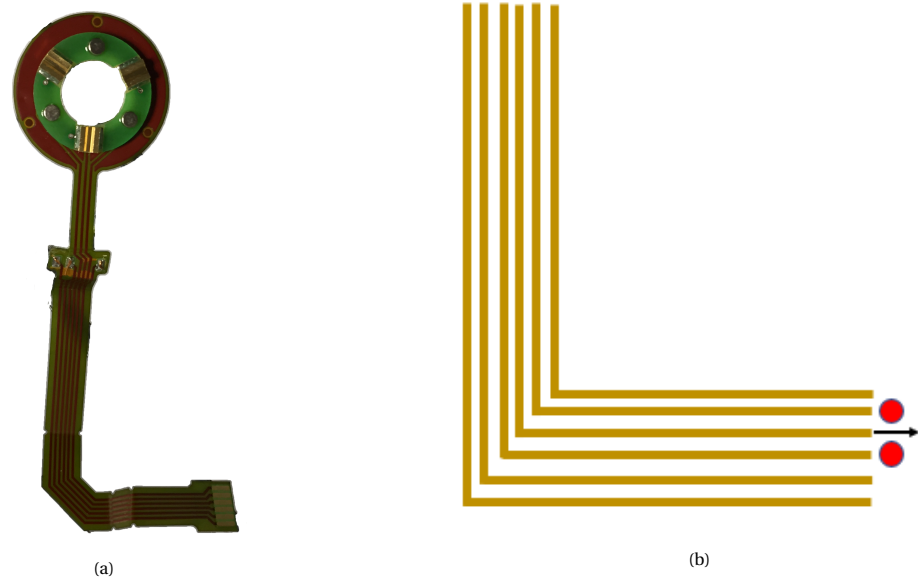


Figure A.4: (a)Flexible printed circuit to provide excitation to the holder (b) Marking of the pins to be connected for input voltage.

The height compensation is realized by three main components inside the vacuum chamber:

- An iron plate attached to the base chamber to which the magnets can easily attach (Part 1 in Figure A.5).
- Magnets underneath the 3-D printed part to affix the 3D printed part to the chamber. (Part 3 in Figure A.5).
- A 3-D printed part to house the FPC. (Part 2 in Figure A.5).

Table A.3: List of parts for height compensation.

Item No	Part Name
1	Iron plate
2	Magnets(10mm dia)
3	3D printed FPC holder

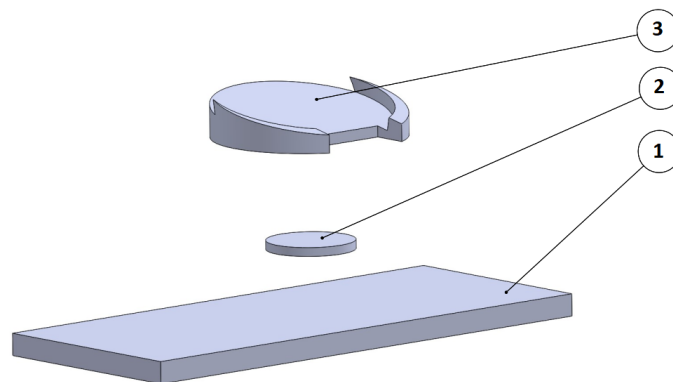


Figure A.5: Three components used to simultaneously increase the height and house the FPC.

A.4. Conclusion

The complete setup can be seen in Figure A.6 wherein the chamber is denoted by the marker 1 and the objective of the laser doppler vibrometer is marked by 2. The pirani gauge which is connected to a push in T fitting in the line from the vacuum pump to the chamber is marked by 3. The gauge is connected to a dual channel measurement and control unit for readout.

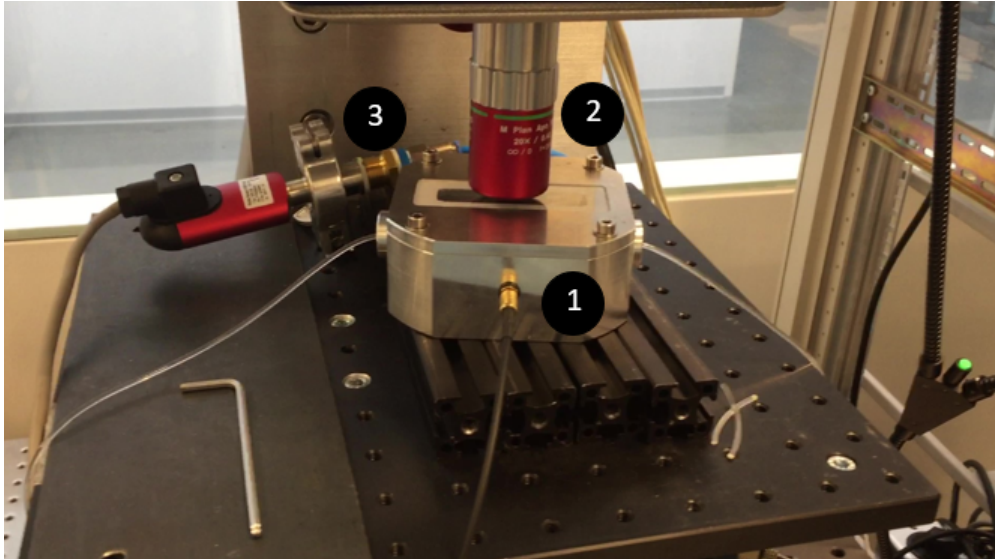


Figure A.6: Final setup connected to all components.

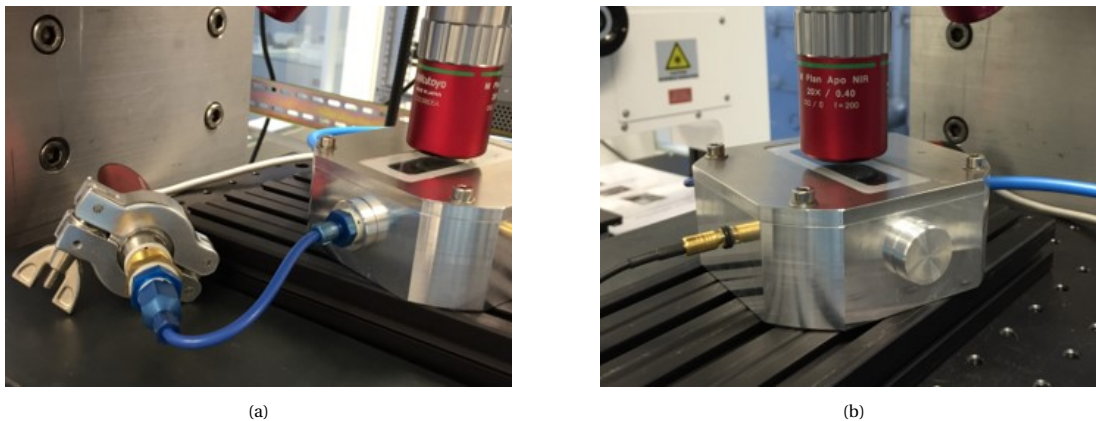


Figure A.7: (a) Connector compatible with vacuum tubing (b) Connector to block the hole in the chamber.

As a final comment, for characterization of the hollow cantilevers in vacuum without fluids, the fluidic connections can be replaced by two alternative connectors:

- One for connecting the Pirani gauge directly to the chamber to measure the vacuum level (Figure A.7 (a)).
- And another to block the hole in the vacuum chamber (Figure A.7 (b)).

This is because the leak from the needles is appreciable and the pressure from the chamber drops from 2.8 to 17 mbar.

B

Interface

As discussed previously, the fluidic interface serves two main purposes:

- To enable the continuous exchange of fluids between the hollow cantilever and the macro-world
- To ensure that the hollow cantilever is appropriately clamped during excitation.

In the two sections that follow we briefly discuss the interfaces designed for the hollow cantilevers used in Chapters 2 and 3 and the interfaces for the new generation of hollow cantilevers for dynamics experiments (more information about these cantilevers can be found in Appendix D).

B.1. Interfaces for two reservoir hollow cantilevers

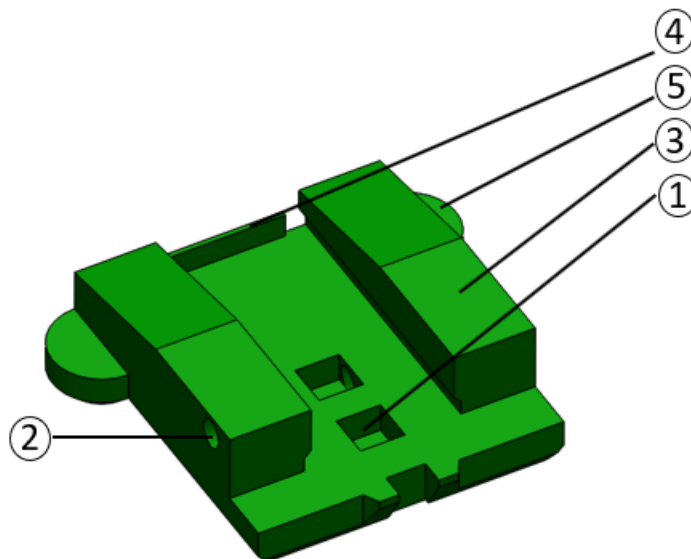


Figure B.1: *Interface for mounting and exchanging fluids with the chip.*

The two reservoirs (marked as 1) seen in the centre (Figure B.1) perfectly align with the reservoirs on the chip. These two reservoirs are connected to the holes (marked as 2) on the raised portions of the interface (marked as 3). Needles can be easily glued into the holes on the raised parts of the interface. The raised portions allow for proper alignment of the chip on the interface and clamping of the interface and chip with the AFM holder clip. The alignment in the other direction is ensured by a raised part at the back of the interface (marked as 4). The shape of the base (marked as 5) portion and its dimensions are such that it can fit into the holder perfectly (Figure B.2).

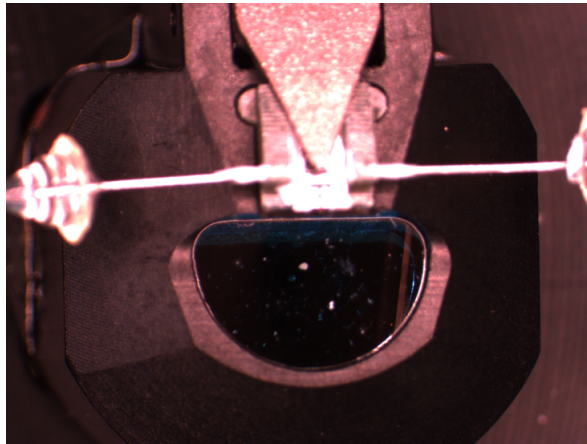


Figure B.2: *Interface with chip mounted on the AFM holder.*

B.2. Interfaces for new generation of two reservoir hollow cantilevers for dynamics experiments

The interfaces used for the new generation of cantilevers have slightly different features (Figure B.3). Since the new chips are bigger than the old chips, the raised portion is smaller in size. The raised portion now hangs outside the base of the interface to ensure that the needles can be inserted properly into the interface. The raised portion at the back is about the same height as that of the chip. The clamping then is done on this raised portion and the chip itself (Figure B.4). The extra area in the front of the interface helps in the gluing as the tweezers can make contact with the interface while placing the chip.

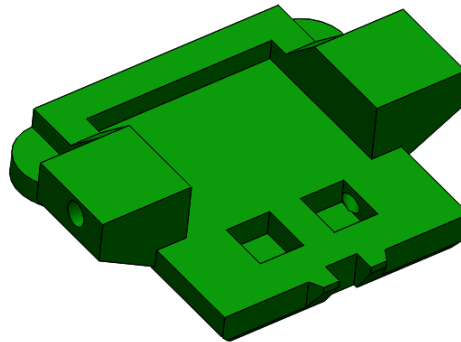


Figure B.3: *Interface for mounting and exchanging fluids with the new chip.*

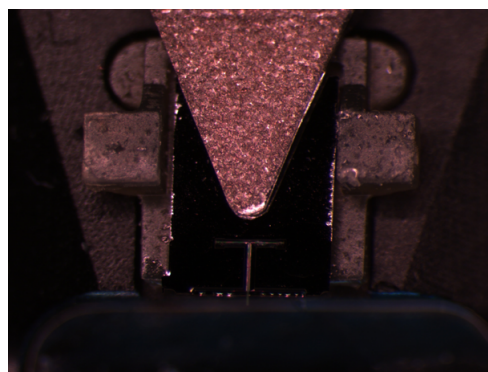


Figure B.4: *Interface with new chip mounted on the AFM holder.*

B.3. Detailed views

B.3.1. Interfaces for two reservoir hollow cantilevers

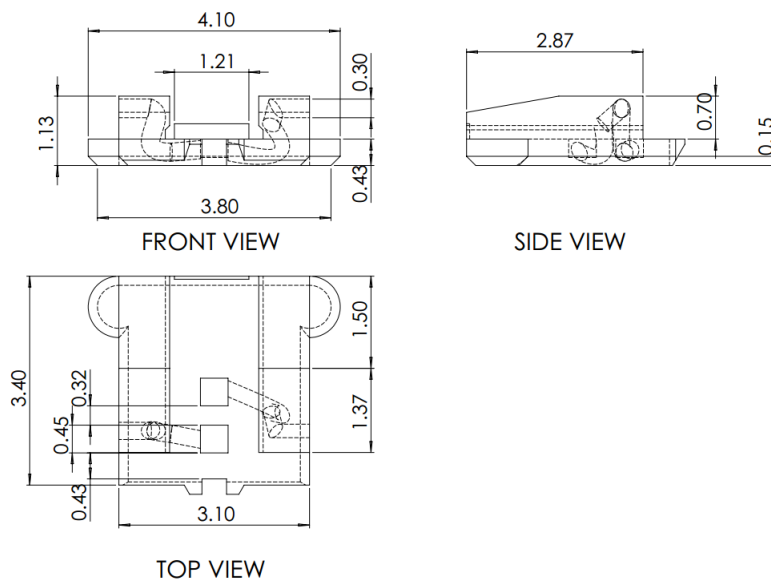


Figure B.5: Orthographic views of the interfaces for the hollow cantilevers. All dimensions are in mm. Scale 1:1.

B.3.2. Interfaces for new generation of two reservoir hollow cantilevers for dynamics experiments

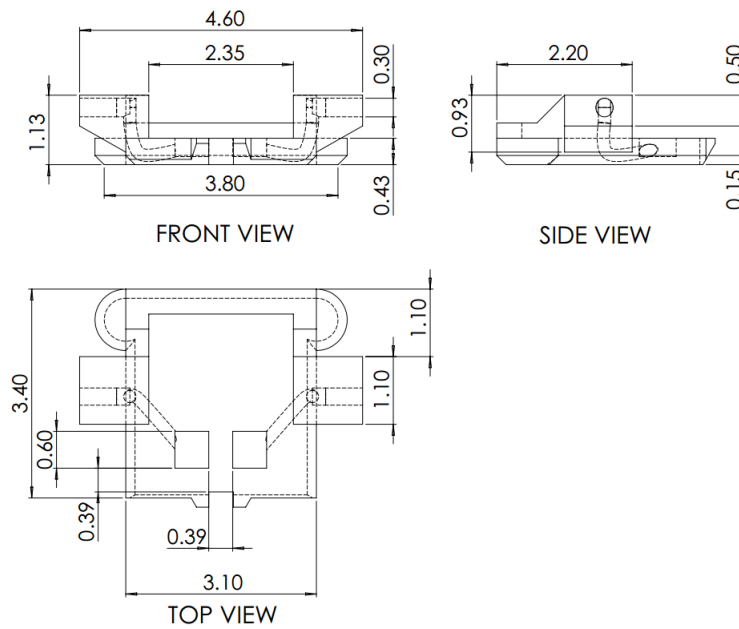


Figure B.6: Orthographic views of the interfaces for the hollow cantilevers for dynamics experiments. All dimensions are in mm. Scale 1:1.

C

Additional Experimental data

In Chapter 2 the shifts in resonance frequency have been plotted for only one of the three experiments conducted. In all further analysis in Chapter 2 data from all three experiments have been used. In this section, the shifts in resonance frequency for the first and second bending modes and the first torsional modes for the other two experiments are plotted. On the y-axis the normalized velocity and the respective phase are plotted. The data from all three experiments has been tabulated in Table C.1.

C.1. Experiment 2

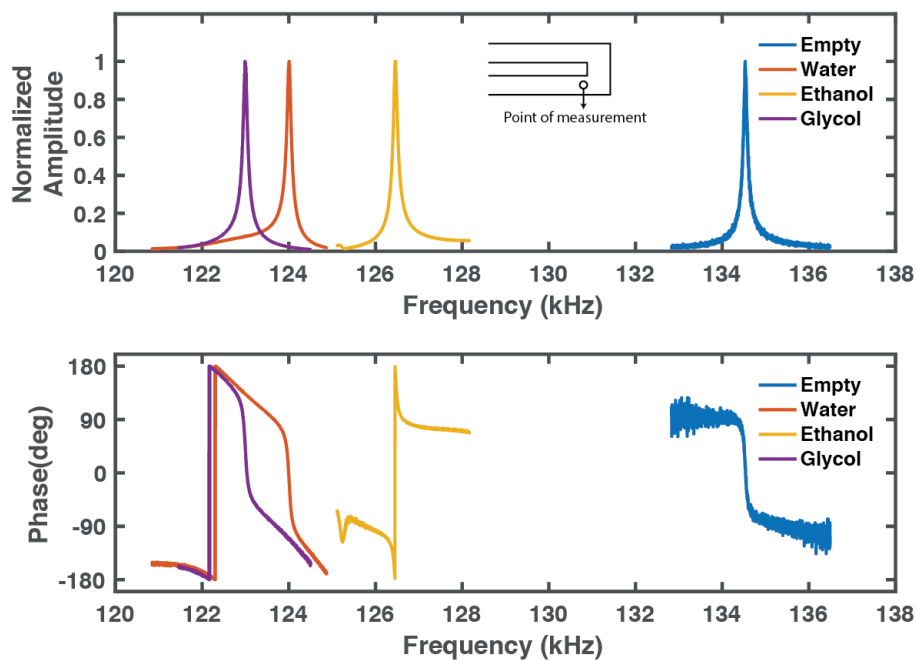


Figure C.1: Resonance frequency shifts for the first bending mode in Experiment 2.

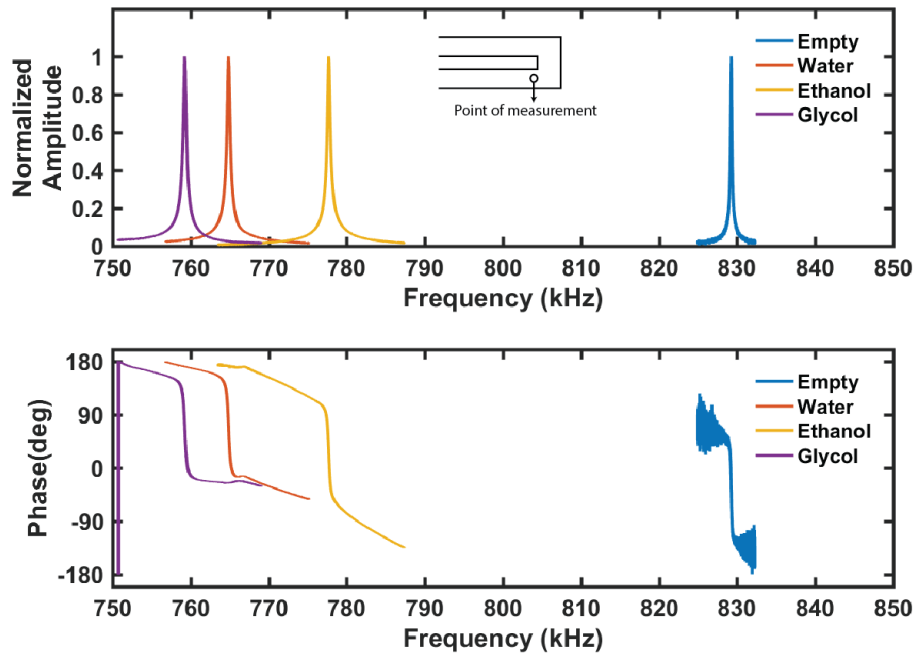


Figure C.2: Resonance frequency shifts for the second bending mode in Experiment 2.

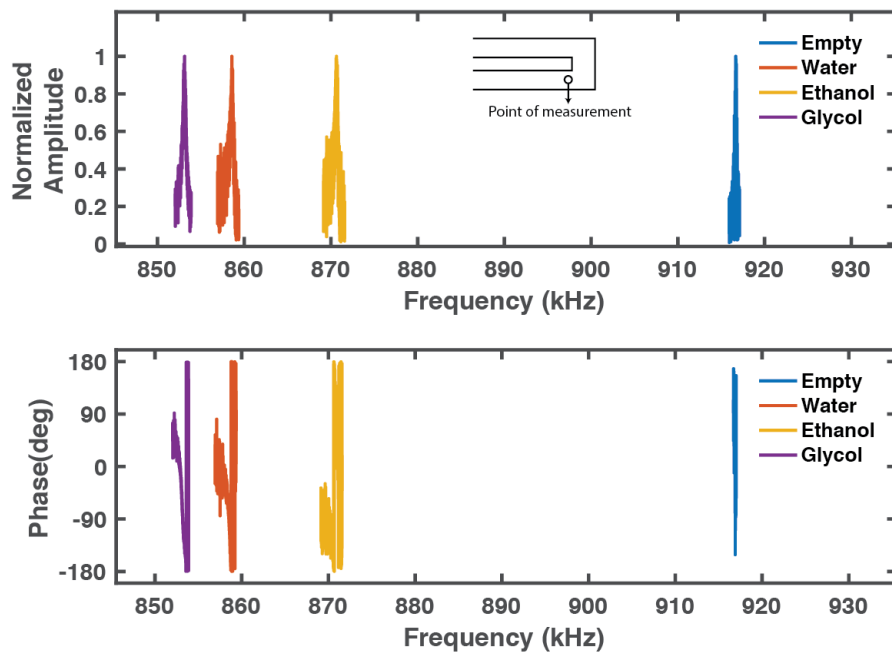


Figure C.3: Resonance frequency shifts for the first torsional mode in Experiment 2.

C.2. Experiment 3

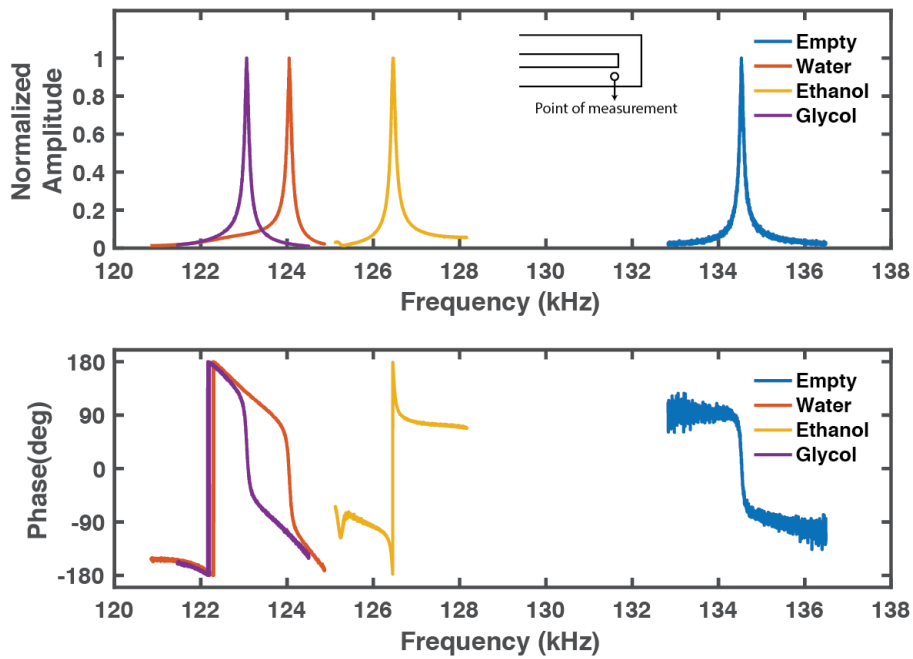


Figure C.4: Resonance frequency shifts for the first bending mode in Experiment 3.

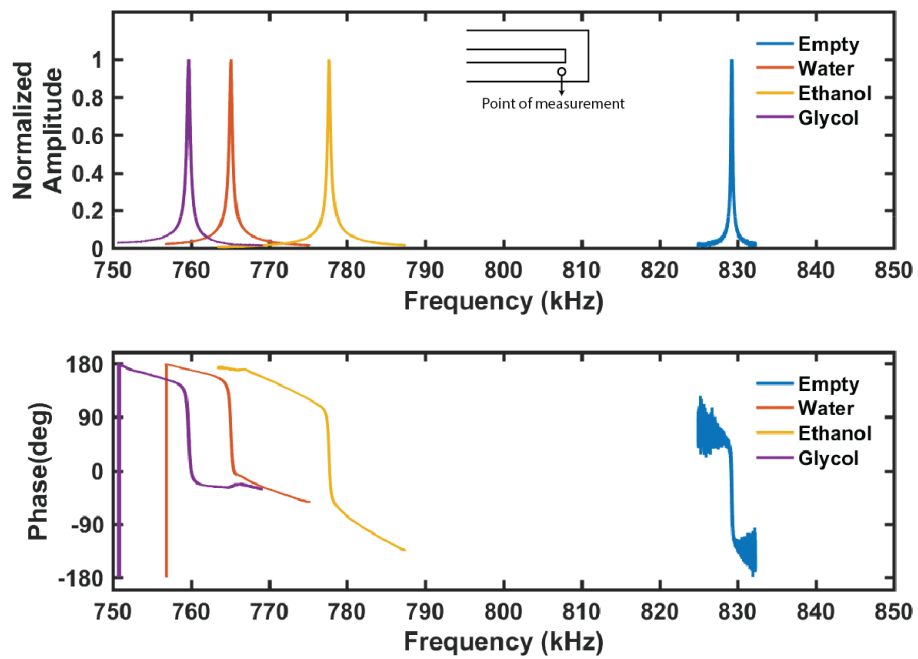


Figure C.5: Resonance frequency shifts for the second bending mode in Experiment 3.

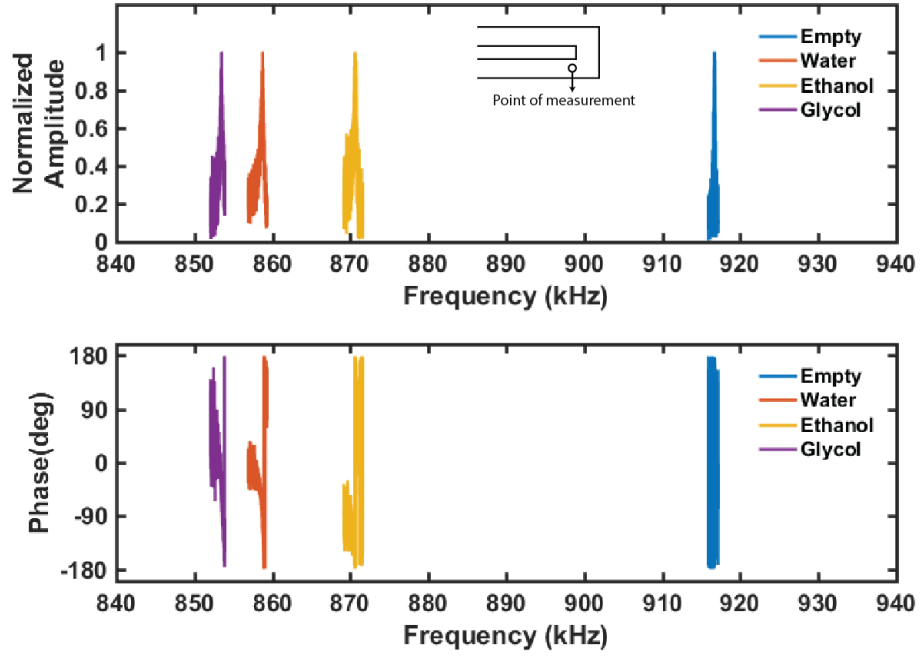


Figure C.6: Resonance frequency shifts for the first torsional mode in Experiment 3.

Table C.1: Resonance frequency (f_{res}) and quality factors (QF) for the first two bending and the first torsional mode for three experiments.

Exp No	Mode No	Empty		Water		Ethanol		Glycol	
		f_{res} (kHz)	QF						
1	1	134.530	1521	123.950	1249	126.423	1265	123.002	1281
2	1			124.007	1233	126.461	1268	122.989	1233
3	1			124.050	1203	126.441	1270	123.063	1249
1	2	829.252	5995	764.635	2091	777.529	2331	759.123	2113
2	2			764.848	2084	777.685	2229	759.257	1938
3	2			765.151	1938	777.625	2229	759.192	1969
1	3	916.674	8374	858.405	2043	870.596	2357	852.846	2502
2	3			858.571	2199	870.639	2458	853.131	2242
3	3			858.729	2105	870.660	2458	853.508	2357

D

Hollow cantilevers for dynamics experiments

After successfully conducting fluid-filling experiments in the two reservoir-hollow cantilevers, it was necessary to fabricate new hollow cantilevers for further experiments. Based on the experience gained while working with the old cantilevers, several improvements were incorporated into the newest generation of devices. The changes are briefly listed below:

D.1. No apertures at the tip of the cantilever

When the hollow cantilevers are used for sensing rather than dispensing it is preferable to not have any apertures (Figure D.1 (a)) at the tip of the cantilever. This allows fluid to directly flow through to the second leg of the cantilever, and prevents the accumulation/loss of fluid through the aperture. It also makes it easier to model the cantilever geometry and calculate or simulate the effects of an added mass/fluid. A smoother channel bend at the tip of the cantilever also facilitates the fluid flow from one leg to another (Figure D.1 (b)).



Figure D.1: (a) Old cantilevers with aperture at tip marked by the red box (b) New cantilevers without aperture at tip. The tip region is marked by the red box. Both images taken at 20X magnification.

D.2. Wider cantilever legs

The lack of an aperture at the tip of the cantilever also makes it easier to position the measurement laser at the tip of the cantilever, as it is at the tip where the vibration amplitude of the cantilever is maximum for the fundamental mode of vibration. Higher amplitudes of vibration are relatively easier to detect compared to smaller amplitudes of vibration.

The laser spot when the cantilever is slightly out of focus is almost as big as the individual leg of the cantilever (Figure D.2(a)). This makes it difficult to position the laser spot on the leg of the cantilever for longer periods, as the measurement laser partly drifts off the cantilever. This can cause the vibrometer to go out of range

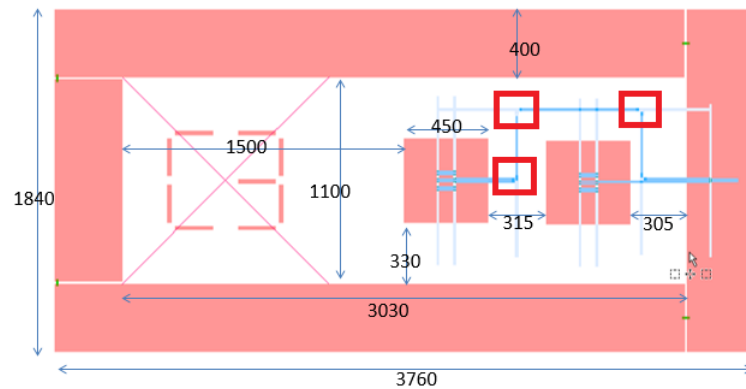
instantaneously. Hence the width of each of the legs is doubled to ensure that the laser can be positioned easily at the beginning of the measurement and over time the measurement laser is still on the leg of the cantilever (Fig D.2(b)).



Figure D.2: (a) Old cantilevers with laser positioned on one leg. Laser point is clearly as wide as the leg of the cantilever. (b) New cantilevers with laser positioned at tip. The laser is now smaller than the width of the leg. Both images taken at 20X magnification.

D.3. Reducing the number of bends of fluidic channels on the chips

In the previous generations of cantilevers the reservoirs were placed one behind another to reduce the total width of the chip. This means that the channels had several sharp bends in order to realize such an optimal geometry, especially in the fluidic path between the cantilever and the outlet reservoir (Fig D.3). The sharp bends caused the fluidic channels to crack at the areas of increased stress concentration. In order to rectify this, the reservoirs are placed side by side and there is only one major bend in the fluidic path from the reservoir to the cantilever. Additionally, the sharpness of the bend has been reduced to reduce stress concentration (Fig D.3). Although, this increases the width of the chip, most of the new chips have no cracks at the bends.



All dimensions in Microns

Figure D.3: Old chip design for hollow cantilevers, the critical areas with respect to stress concentration are marked by the red boxes.

D.4. Different lengths of cantilever

In order to study the changes in sensitivity (change in frequency per unit increase in mass/density) and the changes in quality factor with varying lengths of the cantilever, the wafer has cantilevers of varying lengths. There are six different cantilever lengths with successive cantilever lengths differing by $50\mu\text{m}$. The expected resonance frequency values from simulation for the first four bending modes and the first torsional mode have been tabulated in Table D.1. While determining the lengths of the various cantilevers, separating the torsional and bending resonance frequencies was also a criterion. This was done to avoid interaction of the modes if they are excited in the non-linear regime. The fabricated cantilevers, are actually designed to be 5

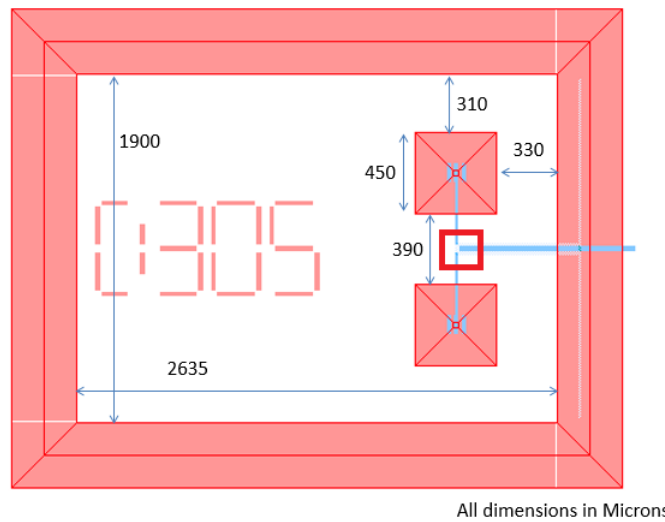
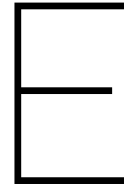


Figure D.4: New chip design for hollow cantilevers, the new bends with large fillet radii are marked by the red boxes.

μm longer than each of the values simulated for. The resonance frequency is not expected to change much for this increase, and must still be in close proximity to these values.

Table D.1: First four bending natural frequencies (f_1 , f_2 , f_3 and f_4) and the first torsional mode frequency (f -tors) for cantilevers with varying lengths simulated from COMSOL.

Length	Width	Thickness	f_1	f_2	f_3	f_4	f -tors
50 μm	26 μm	4.9 μm	2.15 MHz	12.2 MHz	28.6 MHz	46.69 MHz	17.1 MHz
100 μm	26 μm	4.9 μm	563 kHz	3.47 MHz	9.29 MHz	16.9 MHz	2.88 MHz
150 μm	26 μm	4.9 μm	255 kHz	1.59 MHz	4.37 MHz	8.29 MHz	1.50 MHz
200 μm	26 μm	4.9 μm	144 kHz	906 kHz	2.59 MHz	4.85 MHz	942 kHz
250 μm	26 μm	4.9 μm	92 kHz	583 kHz	1.63 MHz	3.17 MHz	636 kHz
300 μm	26 μm	4.9 μm	63 kHz	402 kHz	1.12 MHz	2.20 MHz	451 kHz



Resonance frequency of hollow cantilevers with increasing laser power

Since, we use the laser doppler vibrometer, it is not easy to modulate the laser power on the beam without the addition of optical elements to tune the laser power. We however can change the signal strength of the laser, by moving the cantilever slightly in and out of focus. Although this method of tuning laser strength is not reproducible, we can get an indication of what ratio of laser signal compared to the full laser signal we are using on the interferometer signal (this error has been accounted for in the plots that follow). We decrease the laser signal from the full level, that is generally used to perform measurements, to three lower laser powers: half the full laser power, one-third of the full laser power and one-fifth of the full laser power. The change in resonance frequency of the first, second bending modes and first torsional mode with increasing laser power can be seen below in Figures E.1 , E.2 and E.3 respectively. We perform these experiments at a single point on the cantilever close to the tip.

We observe that for the first two bending modes and the first torsional mode the frequency reduces as we decrease the power. We explain the effect that we observe in Chapter 3.

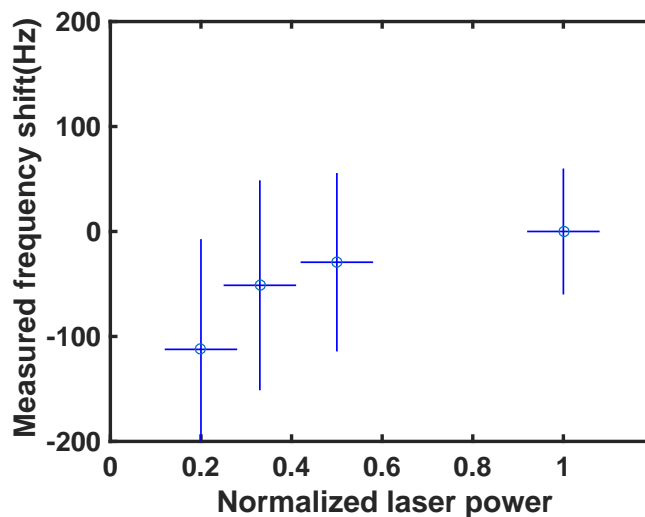


Figure E.1: Shift in resonance frequency (measured) for the first mode plotted vs increasing laser power signal (Error bars along x-axis show uncertainty in tuning laser power). The reference frequency is assumed to be the frequency measured with maximum laser power.

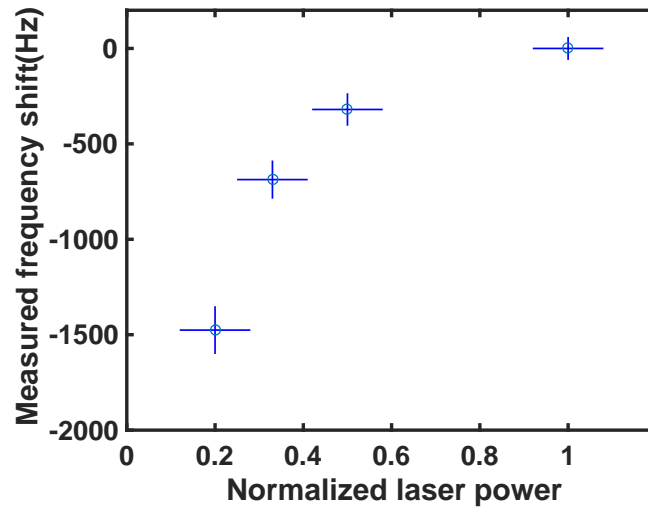


Figure E.2: Shift in resonance frequency (measured) for the second mode plotted vs increasing laser power signal (Error bars along x-axis show uncertainty in tuning laser power). The reference frequency is assumed to be the frequency measured with maximum laser power.

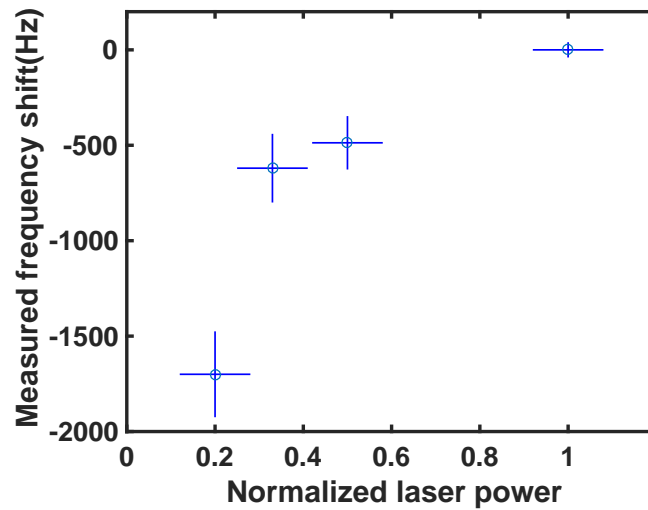
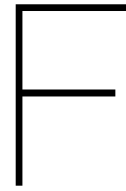


Figure E.3: Shift in resonance frequency (measured) for the first torsional mode plotted vs increasing laser power signal (Error bars along x-axis show uncertainty in tuning laser power). The reference frequency is assumed to be the frequency measured with maximum laser power.



Testing of AFM cantilevers in vacuum

We test standard AFM contact mode cantilevers to confirm that mode shape imaging is possible with our setup in vacuum. The mode shapes Figure E1-Figure E7 linked with the peaks in the average spectrum can be seen below. Here we clearly see that the peaks of the average spectrum are as expected(Lorentzian) (Figure E2 - Figure E8). The frequencies and quality factors measured for each mode have been tabulated in Table E1 .

Table E1: Resonant frequencies and quality factors of contact mode AFM cantilevers.

Mode	Resonance freq	Quality factor
First bending	14.12 kHz	309
Second bending	88.92 kHz	1416
Third bending	249.54 kHz	2720
Fourth bending	489.63 kHz	5220

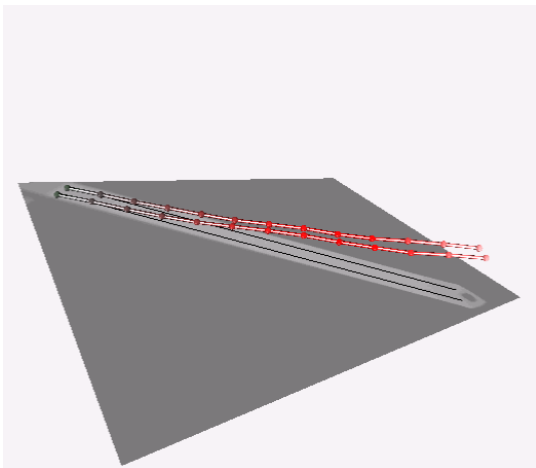


Figure E1: Mode shape corresponding to Mode 1 in vacuum - AFM cantilever.

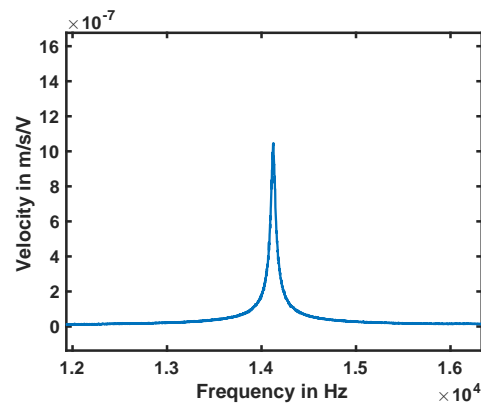


Figure E2: Average spectrum zoomed in at Mode 1 in vacuum - AFM cantilever.

If we observe the resonance frequency differences when we use the laser scan to scan along the length of the cantilever (close to the edges), we see the following maximum differences (experiment performed three times and maximum values reported) in resonance frequency between the points:

- At 14.1 kHz (first bending mode) - A maximum difference of 21.979 Hz between the points excluding the point closest to the base, where the frequency increases by 200 Hz, which is expected because we expect the cantilever to be the stiffest at that location in the first mode.

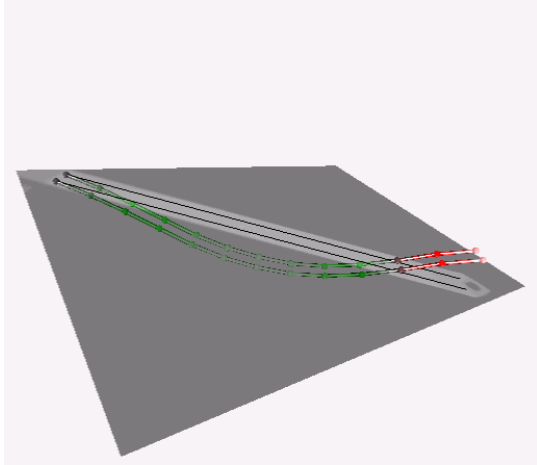


Figure F3: Mode shape corresponding to Mode 2 in vacuum - AFM cantilever.

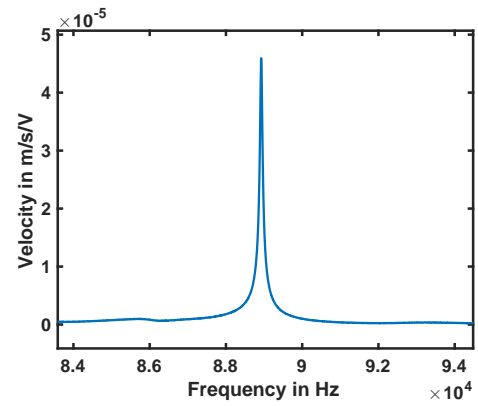


Figure F4: Average spectrum zoomed in at Mode 2 in vacuum - AFM cantilever.

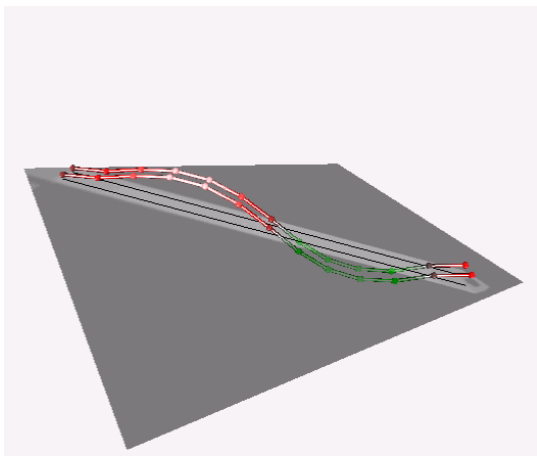


Figure F5: Mode shape corresponding to Mode 3 in vacuum - AFM cantilever.

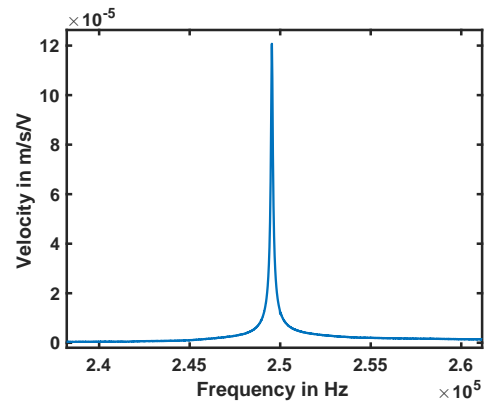


Figure F6: Average spectrum zoomed in at Mode 3 in vacuum - AFM cantilever.

- At 88.9 kHz (second bending mode) - A maximum difference of 85.8594 Hz
- At 249.5 kHz (third bending mode) - A maximum difference of 26.8594 Hz.
- At 489.6 kHz (fourth bending mode) - A maximum difference of 57.3438 Hz

These values are quite comparable to the noise level in our systems (Chapter 2) and hence it is difficult to say much about these values, except that the small differences (compared to a few kHz in hollow cantilevers) in resonance frequencies along the length is within acceptable limits.

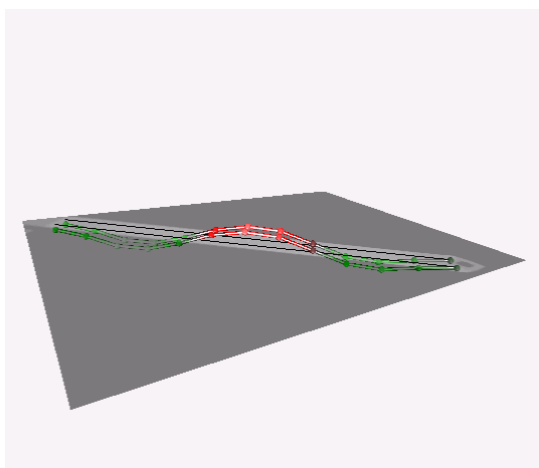


Figure F7: Mode shape corresponding to Mode 4 in vacuum - AFM cantilever.

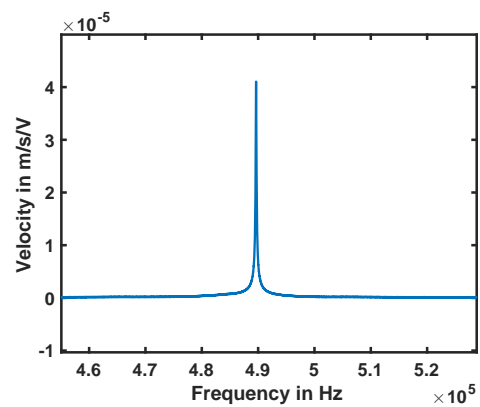


Figure F8: Average spectrum zoomed in at Mode 4 in vacuum - AFM cantilever.



Biomechanical sensors

- NW - The conductance of these devices — which are made from semiconductor nanowires and carbon nanotubes — changes when a target molecule binds to the surface of the device [21].
- MRR - Consists of a high-finesse toroidal optical resonator coupled evanescently to an optical fibre. Adsorption of analytes to the surface of the resonator measurably alters its properties [21].
- QCM-These are centimetre-scale mechanical resonators that can measure the inertial mass of analytes accreting on their surfaces in vacuum, gas or fluid. A downshift in the resonant frequency occurs with target accretion, which is most reliably tracked electronically, in real time [21].
- LFA - A liquid sample (or its extract) containing the analyte of interest moves without the assistance of external forces (capillary action) through various zones of polymeric strips, on which molecules that can interact with the analyte are attached [46].
- SPR- Surface Plasmon Resonance (SPR) is a physical process that occurs when plane-polarized light hits a thin metal film under total internal reflection conditions. SPR biosensors measure the change in refractive index of the solvent near the surface that occurs during complex formation or dissociation of molecules [47].
- BBA - The barcode assay is a sensitive strategy that takes advantage of short oligonucleotides as surrogate targets in biological detection [48].
- IFA - Immunofluorescence (IF) or cell imaging techniques rely on the use of antibodies to label a specific target antigen with a fluorescent dye (also called fluorophores) fluorochromes) such as fluorescein isothiocyanate (FITC) which facilitates visualization of the target distribution in the sample under a fluorescent microscope [49].

Bibliography

- [1] Amir Syahir, Kenji Usui, Kin-ya Tomizaki, Kotaro Kajikawa, and Hisakazu Mihara. Label and label-free detection techniques for protein microarrays. *Microarrays*, 4(2):228–244, 2015. ISSN 2076-3905. doi: 10.3390/microarrays4020228. URL <http://www.mdpi.com/2076-3905/4/2/228>.
- [2] T. P. Burg and S. R. Manalis. Suspended microchannel resonators for biomolecular detection. *Applied Physics Letters*, 83(13):2698–2700, 2003. doi: 10.1063/1.1611625. URL <https://doi.org/10.1063/1.1611625>.
- [3] D. F. Wang, G. Zheng, X. Du, J. Chang, and X. Wang. Analytical study of coupling element effect on anchor-limited quality factor in double beam array based sensing devices. *Microsystem Technologies*, 2017. URL <http://dx.doi.org/10.1007/s00542-017-3547-x>.
- [4] A. Husain, J. Hone, Henk W. Ch. Postma, X. M. H. Huang, T. Drake, M. Barbic, A. Scherer, and M. L. Roukes. Nanowire-based very-high-frequency electromechanical resonator. *Applied Physics Letters*, 83(6):1240–1242, 2003. doi: 10.1063/1.1601311. URL <https://doi.org/10.1063/1.1601311>.
- [5] H. B. Peng, C. W. Chang, S. Aloni, T. D. Yuzvinsky, and A. Zettl. Ultrahigh frequency nanotube resonators. *Phys. Rev. Lett.*, 97:087203, Aug 2006. doi: 10.1103/PhysRevLett.97.087203. URL <https://link.aps.org/doi/10.1103/PhysRevLett.97.087203>.
- [6] Thomas Braun, Viola Barwich, Murali Krishna Ghatkesar, Adriaan H. Bredekamp, Christoph Gerber, Martin Hegner, and Hans Peter Lang. Micromechanical mass sensors for biomolecular detection in a physiological environment. *Phys. Rev. E*, 72:031907, Sep 2005. doi: 10.1103/PhysRevE.72.031907. URL <https://link.aps.org/doi/10.1103/PhysRevE.72.031907>.
- [7] Jungchul Lee, Wenjiang Shen, Kris Payer, Thomas P. Burg, and Scott R. Manalis. Toward attogram mass measurements in solution with suspended nanochannel resonators. *Nano Letters*, 10(7):2537–2542, 2010. doi: 10.1021/nl101107u. URL <http://dx.doi.org/10.1021/nl101107u>. PMID: 20527897.
- [8] Y. T. Yang, C. Callegari, X. L. Feng, K. L. Ekinci, and M. L. Roukes. Zeptogram-scale nanomechanical mass sensing. *Nano Letters*, 6(4):583–586, 2006. doi: 10.1021/nl052134m. URL <http://dx.doi.org/10.1021/nl052134m>. PMID: 16608248.
- [9] B. Ilic, H. G. Craighead, S. Krylov, W. Senaratne, C. Ober, and P. Neuzil. Attogram detection using nanoelectromechanical oscillators. *Journal of Applied Physics*, 95(7):3694–3703, 2004. doi: 10.1063/1.1650542. URL <https://doi.org/10.1063/1.1650542>.
- [10] J. Chaste, A. Eichler, J. Moser, G. Ceballos, R. Rurali, and A. Bachtold. A nanomechanical mass sensor with yoctogram resolution. *Nature Nanotechnology*, 7:301, 2012. doi: 10.1038/nnano.2012.42. URL <http://dx.doi.org/10.1038/nnano.2012.42>.
- [11] M. S. Hanay, S. Kelber, A. K. Naik, D. Chi, S. Hentz, E. C. Bullard, E. Colinet, L. Duraffourg, and M. L. Roukes. Single-protein nanomechanical mass spectrometry in real time. *Nature Nanotechnology*, 7:602, 2012. doi: 10.1038/nnano.2012.119. URL <http://dx.doi.org/10.1038/nnano.2012.119>.
- [12] S. Olcum, N. Cermak, S. C. Wasserman, S. K. Christine, H. Atsumi, K. R. Payer, W. Shen, J. Leel, A. M. Belcher, S. N. Bhatia, and S. R. Manalis. Weighing nanoparticles in solution at the attogram scale. *Proceedings of the National Academy of Sciences*, 111(4):1310–1315, 2014. doi: 10.1073/pnas.1318602111. URL <http://www.pnas.org/content/111/4/1310.abstract>.
- [13] J. Moser, J. Güttinger, A. Eichler, M. J. Esplandiú, D. E. Liu, M. I. Dykman, and A. Bachtold. Ultrasensitive force detection with a nanotube mechanical resonator. *Nature Nanotechnology*, 8:493–496, 2013. doi: 10.1038/nnano.2013.97. URL <http://dx.doi.org/10.1038/nnano.2013.97>.

- [14] O.Sahin S. Husale, Henrik H. J. Persson. Dna nanomechanics allows direct digital detection of complementary dna and microrna targets. *Nature*, 462:1075–1078, 2009. doi: 10.1038/nature08626. URL <http://www.ncbi.nlm.nih.gov/pmc/articles/PMC2966338/>.
- [15] Kilho Eom, Harold S. Park, Dae Sung Yoon, and Taeyun Kwon. Nanomechanical resonators and their applications in biological/chemical detection: Nanomechanics principles. *Physics Reports*, 503(4):115 – 163, 2011. ISSN 0370-1573. doi: <https://doi.org/10.1016/j.physrep.2011.03.002>. URL <http://www.sciencedirect.com/science/article/pii/S0370157311000639>.
- [16] Mark M Stevens, Cecile L Maire, Nigel Chou, Mark A Murakami, David S Knoff, Yuki Kikuchi, Robert J Kimmerling, Huiyun Liu, Samer Haidar, Nicholas L Calistri, Nathan Cermak, Selim Olcum, Nicolas A Cordero, Ahmed Idbaih, Patrick Y Wen, David M Weinstock, Keith L Ligon, and Scott R Manalis. Drug sensitivity of single cancer cells is predicted by changes in mass accumulation rate. *Nature Biotechnology*, 34:1161, 2016. doi: 10.1038/nbt.3697. URL <http://dx.doi.org/10.1038/nbt.3697>.
- [17] John Elie Sader. Frequency response of cantilever beams immersed in viscous fluids with applications to the atomic force microscope. *Journal of Applied Physics*, 84(1):64–76, 1998. doi: 10.1063/1.368002. URL <https://doi.org/10.1063/1.368002>.
- [18] P. Belardinelli, M.K. Ghatkesar, U. Staufer, and F. Alijani. Linear and non-linear vibrations of fluid-filled hollow microcantilevers interacting with small particles. *International Journal of Non-Linear Mechanics*, 93(Supplement C):30 – 40, 2017. ISSN 0020-7462. doi: <https://doi.org/10.1016/j.ijnonlinmec.2017.04.016>. URL <http://www.sciencedirect.com/science/article/pii/S002074621630364X>.
- [19] T.P. Burg, M. Godin, S.M. Knudsen, W. Shen, G. Carlson, J.S. Foster, K. Babcock, and S.R. Manalis. Weighing of biomolecules, single cells and single nanoparticles in fluid. *Nature*, 446:1066, 2007. doi: 10.1038/nature05741. URL <http://dx.doi.org/10.1038/nature05741>.
- [20] J. L. Arlett and M. L. Roukes. Ultimate and practical limits of fluid-based mass detection with suspended microchannel resonators. *Journal of Applied Physics*, 108(8):084701, 2010. doi: 10.1063/1.3475151. URL <https://doi.org/10.1063/1.3475151>.
- [21] J.L. Arlett, E.B. Myers, and M.L. Roukes. Comparative advantages of mechanical biosensors. *Nature*, 6: 203, 2011. doi: 10.1038/nnano.2011.44. URL <http://dx.doi.org/10.1038/nnano.2011.44>.
- [22] A. N. Cleland and M. L. Roukes. Noise processes in nanomechanical resonators. *Journal of Applied Physics*, 92(5):2758–2769, 2002. doi: 10.1063/1.1499745. URL <https://doi.org/10.1063/1.1499745>.
- [23] K. L. Ekinci, X. M. H. Huang, and M. L. Roukes. Ultrasensitive nanoelectromechanical mass detection. *Applied Physics Letters*, 84(22):4469–4471, 2004. doi: 10.1063/1.1755417. URL <https://doi.org/10.1063/1.1755417>.
- [24] N.Cermak, S.Olcum, F.F. Delgado, S.C.Wasserman, K.R. Payer, M.A.Murakami, S.M.Knudsen, R.J. Kimmerling, Y.Kikuchi M.M. Stevens, A. Sandicki, M.Ogawa, V.Agache, F.Baleras, D.M. Weinstock, and S.R.Manalis. High-throughput measurement of single-cell growth rates using serial microfluidic mass sensor arrays. *Nature Biotechnology*, 34:1052, 2016. doi: 10.1038/nbt.3666. URL <http://dx.doi.org/10.1038/nbt.3666>.
- [25] M.Godin, F.F. Delgado, S. Son, W.H. Grover, A.K. Bryan, A.Tzur, P. Jorgensen, K.Payer, A.D.Grossman, M.W.Kirschner, and S.R. Manalis. Using buoyant mass to measure the growth of single cells. *Nature Methods*, 7:287, 2010. doi: 10.1038/nmeth.1452. URL <http://dx.doi.org/10.1038/nmeth.1452>.
- [26] M. Reza Nejadnik and Wim Jiskoot. Measurement of the average mass of proteins adsorbed to a nanoparticle by using a suspended microchannel resonator. *Journal of Pharmaceutical Sciences*, 104(2):698 – 704, 2015. ISSN 0022-3549. doi: <https://doi.org/10.1002/jps.24206>. URL <http://www.sciencedirect.com/science/article/pii/S0022354915302094>.
- [27] M.F. Khan, S. Schmid, P.E. Larsen, Z.J. Davis, W. Yan, E.H. Stenby, and A. Boisen. Online measurement of mass density and viscosity of pl fluid samples with suspended microchannel resonator. *Sensors and Actuators B: Chemical*, 185:456 – 461, 2013. ISSN 0925-4005. doi: <https://doi.org/10.1016/j.snb.2013.04.095>. URL <http://www.sciencedirect.com/science/article/pii/S0925400513005285>.

- [28] I. Lee, K. Park, and J. Lee. Note: Precision viscosity measurement using suspended microchannel resonators. *Review of Scientific Instruments*, 83(11):116106, 2012. doi: 10.1063/1.4768245. URL <https://doi.org/10.1063/1.4768245>.
- [29] Thomas P. Burg, John E. Sader, and Scott R. Manalis. Nonmonotonic energy dissipation in microfluidic resonators. *Phys. Rev. Lett.*, 102:228103, Jun 2009. doi: 10.1103/PhysRevLett.102.228103. URL <https://link.aps.org/doi/10.1103/PhysRevLett.102.228103>.
- [30] Murali Krishna Ghatkesar, Ekaterina Rakhmatullina, Hans-Peter Lang, Christoph Gerber, Martin Hegner, and Thomas Braun. Multi-parameter microcantilever sensor for comprehensive characterization of newtonian fluids. *Sensors and Actuators B: Chemical*, 135(1):133 – 138, 2008. ISSN 0925-4005. doi: <https://doi.org/10.1016/j.snb.2008.08.012>. URL <http://www.sciencedirect.com/science/article/pii/S0925400508005522>.
- [31] S. Schmid, Villanueva L.G., and Roukes M.L. *Fundamentals of Nanomechanical Resonators*. 2016. doi: 10.1007/978-3-319-28691-4. URL <https://link.springer.com/book/10.1007/978-3-319-28691-4>.
- [32] J.E. Sader, T.P. Burg, and S. R. Manalis. Energy dissipation in microfluidic beam resonators. *Journal of Fluid Mechanics*, 650:215–250, 2010. doi: 10.1017/S0022112009993521.
- [33] Gerhard Meyer and Nabil M. Amer. Novel optical approach to atomic force microscopy. *Applied Physics Letters*, 53(12):1045–1047, 1988. doi: 10.1063/1.100061. URL <https://doi.org/10.1063/1.100061>.
- [34] N Liu, F. Giesen, M. Belov, J. Losby, J. Moroz, A. E. Fraser, G. McKinnon, T. J. Clement, V. Sauer, W. K. Hiebert, and M. R. Freeman. Time-domain control of ultrahigh-frequency nanomechanical systems. *Nature Nanotechnology*, 3, 2008. doi: 10.1038/nnano.2008.319. URL <http://dx.doi.org/10.1038/nnano.2008.319>.
- [35] A. Labuda, T. Brastaviceanu, I. Pavlov, W. Paul, and D. E. Rassier. Optical detection system for probing cantilever deflections parallel to a sample surface. *Review of Scientific Instruments*, 82(1):013701, 2011. doi: 10.1063/1.3527913. URL <https://doi.org/10.1063/1.3527913>.
- [36] M. Sansa, E. Sage, E.C. Bullard, M. Gely, Thomas Alava, A.K. Naik, L.G. Villanueva, L. Duraffourg, M.L. Roukes, G. Jourdan, and S. Hentz. Frequency fluctuations in silicon nanoresonators. *Nature Nanotechnology*, 11, 2016. doi: <http://dx.doi.org/10.1038/nnano.2016.19>. URL <http://dx.doi.org/10.1038/nnano.2016.19>.
- [37] Hamed Sadeghian, Chung-Kai Yang, Khashayar Babaei Gavan, Johannes F L Goosen, Emile W J M van der Drift, Herre S J van der Zant, Andre Bossche, Paddy J French, and Fred van Keulen. Some considerations of effects-induced errors in resonant cantilevers with the laser deflection method. *Journal of Micromechanics and Microengineering*, 20(10):105027, 2010. URL <http://stacks.iop.org/0960-1317/20/i=10/a=105027>.
- [38] Felipe Aguilar Sandoval, Mickael Geitner, Éric Bertin, and Ludovic Bellon. Resonance frequency shift of strongly heated micro-cantilevers. *Journal of Applied Physics*, 117(23):234503, 2015. doi: 10.1063/1.4922785. URL <https://doi.org/10.1063/1.4922785>.
- [39] O. Marti, A. Ruf, M. Hipp, H. Bielefeldt, J. Colchero, and J. Mlynek. Mechanical and thermal effects of laser irradiation on force microscope cantilevers. *Ultramicroscopy*, 42-44:345 – 350, 1992. ISSN 0304-3991. doi: [https://doi.org/10.1016/0304-3991\(92\)90290-Z](https://doi.org/10.1016/0304-3991(92)90290-Z). URL <http://www.sciencedirect.com/science/article/pii/030439919290290Z>.
- [40] T Larsen, S Schmid, S Dohn, J E Sader, A Boisen, and L G Villanueva. Position and mode dependent optical detection back-action in cantilever beam resonators. *Journal of Micromechanics and Microengineering*, 27(3):035006, 2017. URL <http://stacks.iop.org/0960-1317/27/i=3/a=035006>.
- [41] S Miura Matsuda, M. H. Hara, Michio Miura, Takashi Matsuda, Masanori Ueda, Yoshio Satoh, and Kenya Hashimoto. Correlation between temperature coefficient of elasticity and fourier transform infrared spectra of silicon dioxide films for surface acoustic wave devices. *IEEE Transactions on Ultrasonics, Ferroelectrics and Frequency Control*, 58, 2011.

- [42] J. Lee, R. Chunara, W. Shen, K. Payer, K. Babcock, T. P. Burg, and S. R. Manalis. Suspended microchannel resonators with piezoresistive sensors. *Lab Chip*, 11:645–651, 2011. doi: 10.1039/C0LC00447B. URL <http://dx.doi.org/10.1039/C0LC00447B>.
- [43] William E. Newell. Miniaturization of tuning forks. *Science*, 161(3848):1320–1326, 1968. ISSN 0036-8075. doi: 10.1126/science.161.3848.1320. URL <http://science.sciencemag.org/content/161/3848/1320>.
- [44] M. Li, H.X. Tang, and M.L. Roukes. Ultra-sensitive nems-based cantilevers for sensing, scanned probe and very high-frequency applications. *Nature Nanotechnology*, 2, 2007. doi: 10.1038/nnano.2006.208. URL <http://dx.doi.org/10.1038/nnano.2006.208>.
- [45] S. Olcum, N. Cermak, S.C. Wasserman, and S.R. Manalis. High-speed multiple-mode mass-sensing resolves dynamic nanoscale mass distributions. *Nature Communications*, 6, 2015. doi: 10.1038/ncomms8070. URL <http://dx.doi.org/10.1038/ncomms8070>.
- [46] P. Estrela, K.M. Koczula, and A. Gallotta. Lateral flow assays. *Essays in Biochemistry*, 60:111–120, 2016. ISSN 2076-3905. doi: 10.1042/EBC20150012. URL <http://www.ncbi.nlm.nih.gov/pmc/articles/PMC4986465/>.
- [47] Rebecca L Rich and David G Myszka. Advances in surface plasmon resonance biosensor analysis. *Current Opinion in Biotechnology*, 11(1):54 – 61, 2000. ISSN 0958-1669. doi: 10.1016/S0958-1669(99)00054-3. URL <http://www.sciencedirect.com/science/article/pii/S0958166999000543>.
- [48] C. Zhang, Z. Jiang, Y. Zhang, P. Zou, Y. She, F. Jin, H. Shao S. Wang, L. Zheng, and J. Wang. A competitive bio-barcode amplification immunoassay for small molecules based on nanoparticles. *Scientific Reports*, 6:38114, 2016. doi: 10.1038/srep38114. URL <http://dx.doi.org/10.1038/srep38114>.
- [49] Abcam Website. Direct vs indirect immunofluorescence, 2017. URL <http://www.abcam.com/secondary-antibodies/direct-vs-indirect-immunofluorescence>.